

Buoyancy driven convection in vertically shaken granular matter: experiment, numerics, and theory

Peter Eshuis · Ko van der Weele · Meheboob Alam · Henk Jan van Gerner ·
Martin van der Hoef · Hans Kuipers · Stefan Luding ·
Devaraj van der Meer · Detlef Lohse

Received: 3 June 2012 / Published online: 24 August 2013
© Springer-Verlag Berlin Heidelberg 2013

Abstract Buoyancy driven granular convection is studied for a shallow, vertically shaken granular bed in a quasi 2D container. Starting from the granular Leidenfrost state, in which a dense particle cluster floats on top of a dilute gaseous layer of fast particles (Meerson et al. in *Phys Rev Lett* 91:024301, 2003; Eshuis et al. in *Phys Rev Lett* 95:258001, 2005), we witness the emergence of counter-rotating convection rolls when the shaking strength is increased above a critical level. This resembles the classical onset of convection—at a critical value of the Rayleigh number—in a fluid heated from below. The same transition, even quantitatively, is seen in molecular dynamics simulations, and explained by a hydrodynamic-like model in which the granular material is treated as a continuum. The critical shaking strength for the onset of granular convection is accurately reproduced

by a linear stability analysis of the model. The results from experiment, simulation, and theory are in good agreement. The present paper extends and completes our earlier analysis (Eshuis et al. in *Phys Rev Lett* 104:038001, 2010).

Keywords Shaken granular matter · Granular gas · Leidenfrost state

1 Introduction

Granular materials in many instances exhibit fluid-like behavior, and it is therefore no wonder that much effort has been devoted during the past few decades to arrive at a hydrodynamic description in which these materials are treated as a continuous medium [1–11]. Indeed, one of the key questions in granular research today is to what extent continuum theory can describe the plethora of new and often counter-intuitive phenomena [9, 12–15]. It has become clear that a variety of phenomena such as clustering [16–20], Couette and chute flow [21–23] and granular jets [24, 25] indeed admit a quantitative description in terms of hydrodynamic-like models. This is important not only from a fundamental point of view—revealing the physical mechanisms behind the collective behavior of the particles, all the more remarkable when one realizes that the particles are not bound to each other by any adhesive forces—but also for innumerable applications in industry. As an example we mention fluidized beds, widely used in the chemical industry and typically tens of meters high, for which a direct calculation of all the individual particle trajectories is simply out of the question [26]. Here the continuum description is a welcome, and even necessary, alternative.

In the present paper, which is an extended version of our earlier publication [27], we apply the hydrodynamic

P. Eshuis · H. J. van Gerner · M. van der Hoef · D. van der Meer ·
D. Lohse (✉)
Physics of Fluids & MESA + Research Institute,
University of Twente, P.O. Box 217,
7500 AE Enschede, The Netherlands
e-mail: d.lohse@utwente.nl

K. van der Weele
Mathematics Department,
University of Patras, 26500 Patras, Greece

M. Alam
Engineering Mechanics Unit, Jawaharlal Nehru Center
for Advanced Scientific Research, Jakkur P.O.,
Bangalore 560064, India

H. Kuipers
Fundamentals of Chemical Reaction Engineering,
Technical University of Eindhoven, Eindhoven,
The Netherlands

S. Luding
Multi Scale Mechanics, University of Twente, P.O. Box 217,
7500 AE Enschede, The Netherlands

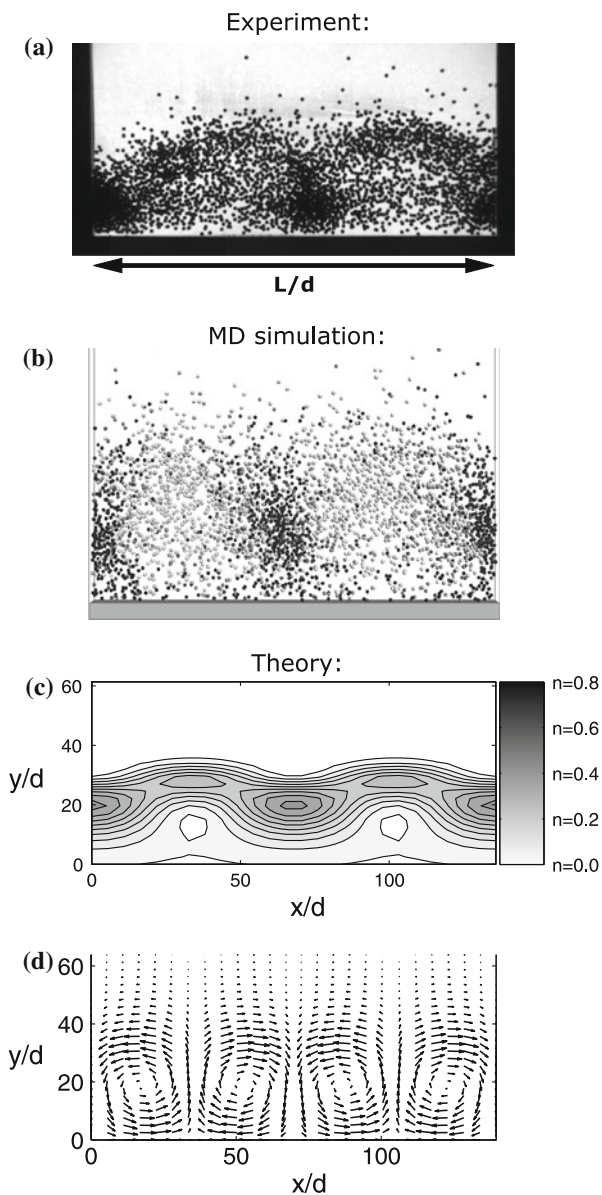


Fig. 1 Experiment, MD simulation, and theory: **a** The quasi 2D experimental setup showing granular convection for $F = 6.2$ layers of $d = 1.0$ mm steel beads shaken at $a = 3.0$ mm and $f = 55.0$ Hz (dimensionless shaking strength $S = 110$). The adjustable container length is $L/d = 101$ in this experiment. Two convective cells are present here, each consisting of a pair of counter-rotating rolls. The beads move up in the dilute regions (high granular temperature) and are sprayed sideways to the three dense clusters (low granular temperature). The sidewalls induce a downward motion due to the extra dissipation, so we always find a cluster at the wall. Available as movie 1a with the online version of the paper. **b** Molecular dynamics simulation matching the experimental parameters from above, i.e. $F = 6.2$ particle layers shaken at $a = 3.0$ mm and $f = 55$ Hz ($S = 110$). The light colored particles are moving upward and the dark ones downward. Available as movie 1b with the online version of the paper. **c** The density profile according to our hydrodynamic theory for $F = 6$ layers and a dimensionless shaking strength of $S = 110$. The color coding indicates the regions with high density (black) and low density (white). **d** The corresponding theoretical velocity profile showing two pairs of counter-rotating convection rolls

approach to buoyancy driven convection in a strongly shaken granular bed, see Fig. 1. Taking as a starting point the granular Leidenfrost state¹, in which a dense cluster is elevated by a gas-like layer of fast particles underneath [28], we find—when the shaking strength is increased beyond a certain threshold value—that this state becomes unstable and gives way to a pattern of convection rolls [29]. These rolls are very reminiscent of the well-known Rayleigh-Bénard convection rolls in an ordinary fluid, when this is heated from below and the temperature gradient exceeds a certain critical value [30–37]. In the ordinary case, the ascending part of the roll contains hot fluid (which goes upward thanks to its smaller density) and the descending part of the roll contains relatively cool, denser fluid. Likewise, in the granular case, highly mobile particles move up in the dilute regions, are then sprayed sideways towards denser regions, where they collectively move downwards. The resemblance is indeed so strong that we will model the granular convection in analogy with the hydrodynamic theory known from Rayleigh-Bénard convection, adapting it where necessary to the granular context. Experiment, numerical simulation, and theoretical analysis are used side by side to supplement and reinforce each other. Together these three will provide a comprehensive picture of the convection.

Convection is widespread in vibrated granular systems, and it plays an important role e.g. in the famous Brazil nut effect [38]. In that case, however, the bed is fluidized only *mildly*, without any pronounced density differences, and the rolls emerge mainly as a result of the interaction between the particles and the walls of the container. That is, the convection is boundary-driven. Almost all studies up to date are dealing with this type of convection [38–50, 52–54, 56–63]. However, buoyancy-driven granular convection can also occur without direct wall interaction as origin, as was first observed in the event-driven MD simulations by Ramírez et al. [51] and Isobe [64] and later by He et al. [55].

Here we will be concerned with buoyancy-driven convection, which appears at *strong* fluidization, in the presence of considerable density differences. This is a bulk effect and is only marginally influenced by the boundaries. This type of convection has been reported much more rarely in the literature: We are aware of one theoretical study by [65], one numerical study by [66], while the first experimental observation of buoyancy-driven granular convection was presented in [29].

Khain and Meerson [65] studied an infinite two-dimensional horizontal layer with a (fully elastic) closed top. By contrast, our experiment has an open surface. However, just as Khain and Meerson we start our analysis from the

¹ Meerson et al. [71] had numerically predicted such a state 2 years prior to its experimental observation by Eshuis et al. [27]. Meerson et al. called the state ‘floating cluster’.

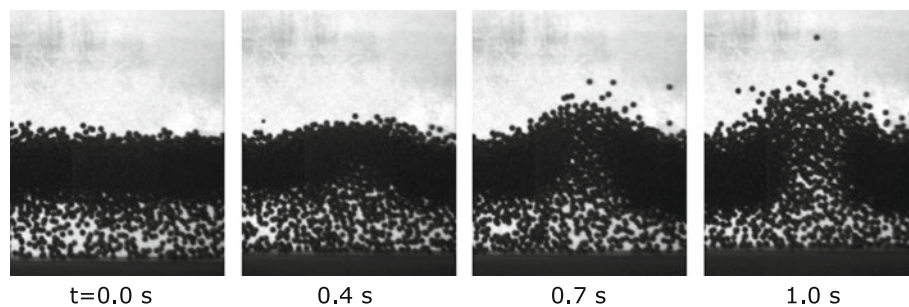


Fig. 2 Experiment: Breakthrough of a convection roll for $F = 11.1$ layers of steel beads shaken at an amplitude of $a = 3.0$ mm and frequency $f = 45$ Hz (dimensionless shaking strength $S = 75$). These pictures show approximately one-third of the total container length $L/d = 101$, close to the right wall, from an experiment in which the

experimentally observed inhomogeneous Leidenfrost state in which a solid phase co-exists with a gaseous phase [28], see Fig. 2. One difference between that work and ours is that in Khain and Meerson’s case there can be granular convection rolls without any density inversion, whereas here we focus on the case of convection rolls with prior density inversion. The most important difference between our work and that one by Khain and Meerson [65] is that we account for finite-density corrections to the constitutive relations of the granular hydrodynamics.

In the numerical model by Paolotti et al. the container walls were taken to be perfectly elastic, leading to convection patterns in which the rolls are either moving up or down along the sidewalls. In our system, with dissipative walls, they always move down (see Fig. 1). Another difference is that the convection rolls studied by [66] emerge as instabilities from a state of homogeneous density rather than from the Leidenfrost state.

In the present paper we will stay close to the experiments reported in [29], both in the molecular dynamics (MD) simulations and in the model. As we will see, the observed onset of convection can be quantitatively explained by a linear stability analysis around the Leidenfrost state.

The paper is organized as follows: In Sect. 2 we introduce the setup and give the main experimental results, followed in Sect. 3 by a description of our code used in the MD simulations. In Sect. 4 we develop the hydrodynamic model and derive the equations plus boundary conditions on which we then proceed to perform the stability analysis. The theoretically determined value of the shaking strength beyond which granular convection sets in is found to be in perfect agreement with experiment and MD simulation. The comparison between experiment, numerics, and theory is continued in Sect. 5, where we compare the density, velocity, and (granular) temperature fields as observed by all three methods. Again we find good agreement. Finally, Sect. 6 contains concluding remarks. The paper is accompanied by two Appendices: The first of these discusses the shear viscosity μ for

our granular system, while the second gives the relations for the pressure, dissipation, and transport coefficients used in the theoretical model.

frequency was linearly increased from $f = 42$ Hz to $f = 48$ Hz at a rate of 90 Hz/min. The breakthrough of the convection roll, starting from the Leidenfrost state, took place in less than 1 s, i.e. $\Delta f < 1.5$ Hz. Note the similarity between this figure and figure 2 of Isobe [64] who performed MD simulations

2 Experimental setup and results

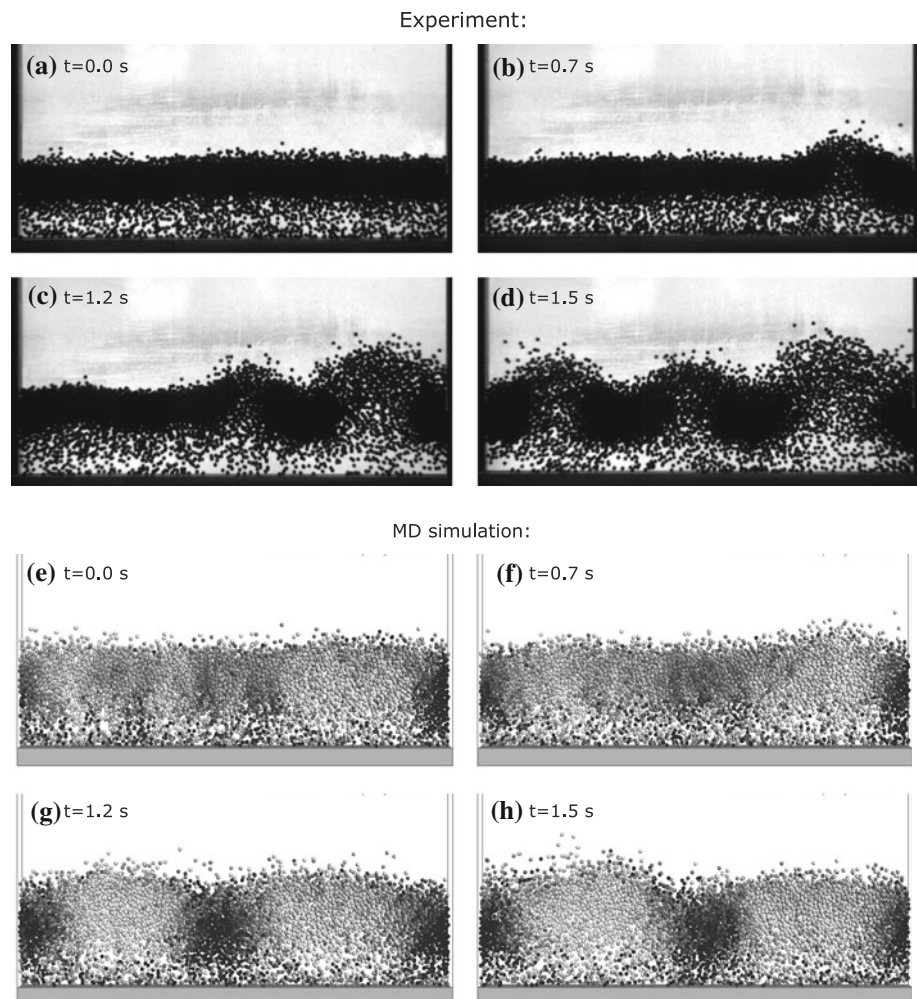
Our experimental setup (Fig. 1) consists of a quasi 2D Perspex container of dimensions $L \times D \times H$ with an adjustable container length $L = 10 - 202$ mm, a depth $D = 5$ mm, and a height $H = 150$ mm. The container is partially filled with steel beads of diameter $d = 1.0$ mm, density $\rho = 7,800$ kg/m³, and coefficient of normal restitution $e \approx 0.9$. The setup is mounted on a sinusoidally vibrating shaker with tunable frequency f and amplitude a . The experiments are recorded with a high-speed camera capturing 2,000 frames per run at a frame rate of 1,000 frames per second.

The natural dimensionless control parameters to analyse the experiments are: (i) the shaking parameter for strong fluidization [28,29,67]:

$$S = \frac{a^2 \omega^2}{gd}, \tag{1}$$

with $\omega = 2\pi f$ and $g = 9.81$ m/s². The shaking strength S is the ratio of the kinetic energy inserted into the system by the vibrating bottom and the potential energy associated with the particle diameter d ; (ii) the number of bead layers F , defined as $F \equiv N_p d^2 / (LD)$, where N_p is the number of particles (determined from the total mass); (iii) the inelasticity parameter $\varepsilon = (1 - e^2)$; and (iv) the aspect ratio L/d . The parameter ε is taken to be constant in this paper, since we ignore the velocity dependence. We use steel beads throughout unless otherwise stated. The aspect ratio L/d is varied in the range of $L/d = 10 - 202$ by adjusting the container length L in steps of 4 mm; So, we will systematically vary all dimensionless parameters (except the inelasticity parameter

Fig. 3 Experiment versus MD simulation: Onset of convection. **a–d** The onset of convection for $F = 11.1$ layers of steel beads in a container of length $L/d = 101$ shaken at an amplitude of $a = 3.0$ mm and frequency $f = 45$ Hz ($S = 75$). The frequency was linearly increased in the range of $f = 42 - 48$ Hz at 90 Hz/min. The transition from the steady Leidenfrost state to fully developed convection took place in 1.5 s, i.e. $\Delta f < 2.3$ Hz. Available as movie 2a with the online version of the paper. **e–h** The breakthrough process in a molecular dynamics simulation equivalent to the experiment: $F = 11.1$, shaking amplitude $a = 3.0$ mm, and linearly increased frequency at 90 Hz/min with $f = 44$ Hz in **e**. The onset of convection takes place at a frequency of $f = 45$ Hz ($S = 75$). Available as movie 2b with the online version of the paper



ε) by changing the amplitude a , the frequency f , the number of layers F and the container length L .

What is the origin of convection in our system? For only a small number of layers convection arises from the bouncing bed base state (where the granular bed bounces in a similar way as a single particle would do), which occurs for relatively weak fluidization [29]. The vastly more typical transition to convection is observed for high fluidization and is formed out of the Leidenfrost state, in which a cluster of slow almost immobile particles is supported by a gaseous region of fast particles underneath. Figure 2 shows how a number of particles becomes more mobile (higher granular temperature) than the surrounding ones and creates an opening in the floating cluster of the Leidenfrost state. These particles have picked up an excess of energy from the vibrating bottom (due to a statistical fluctuation) and collectively move upwards, very much like the onset of Rayleigh-Bénard convection in a classical fluid heated from below. This upward motion of the highly mobile beads must be balanced by a downward movement of neighbor-

ing particles, leading to the formation of a convection roll-pair.

The downward motion is most easily accomplished at the sidewalls, due to the extra source of dissipation (i.e. the friction with the walls), and for this reason the first convection roll is always seen to originate near one of the two sidewalls. As shown in Fig. 3, this first roll within a second triggers the formation of rolls along the entire length of the container, leading to a fully developed convection pattern.

To find out how these fully developed convection patterns depend on the dimensionless control parameters, we systematically vary them individually, starting with the aspect ratio L/d .

Figure 4 shows that when the aspect ratio L/d is increased, the number of convection rolls increases. Let k be the number of observed convective cells, each consisting of a pair of counter-rotating rolls. We find that k grows linearly with the aspect ratio L/d , see Fig. 4e. This indicates that the cells have an intrinsic typical length Λ independent of the aspect ratio. This is again similar to the rolls in Rayleigh-Bénard

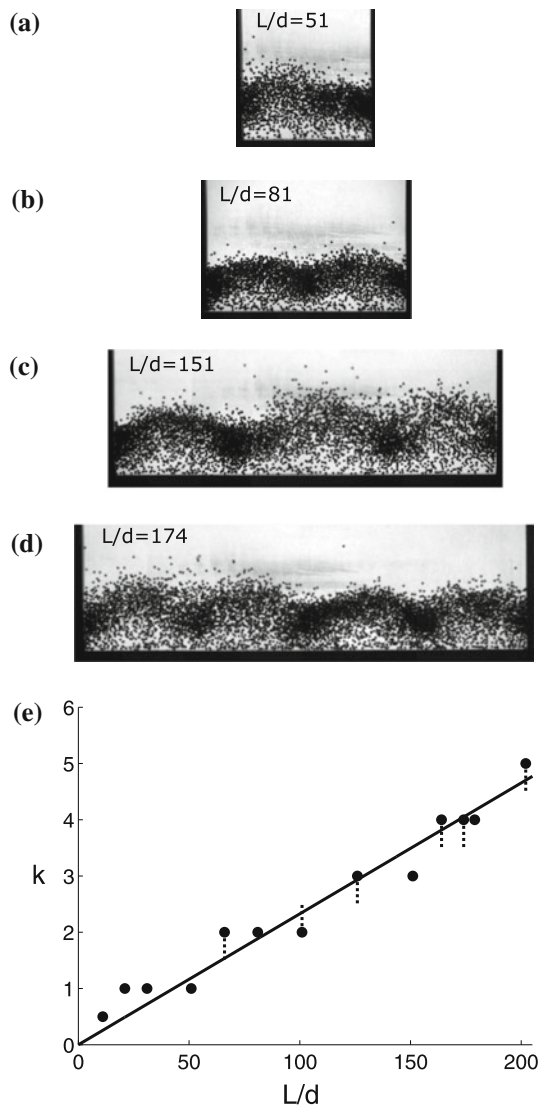


Fig. 4 Experiment: The number of convective cells k for increasing container length L/d , keeping the number of layers fixed at $F = 6.2$ and the shaking strength at $S = 63$ ($a = 2.5$ mm and $f = 50$ Hz): **a** $k = 1$ (one pair of convection rolls), **b** $k = 2$ (two pairs), **c** $k = 3$, **d** $k = 4$. **e** The number of convective cells k as a function of the container length L/d for the same parameter values as in **a–d**. The dotted vertical lines denote a situation in which the system continuously switches between two states with a different number of rolls, as explained in the text. The straight line is a guide to the eyes. The intrinsic cell length Λ for this (S, F) -combination, determined from the linear fit through the data points, is $\Lambda = 43$ mm. Experiments shown in **a–d** are available as movie 3 with the online version of the paper

convection for a normal fluid, which also have an intrinsic length. The “intrinsic” cell length ($\Lambda = 43$ mm for $F = 6.2$ particle layers at a fixed shaking strength $S = 63$) is determined from the linear fit through the experimental data and is indicated by the straight, black line in Fig. 4e.

The dotted vertical lines in Fig. 4e represent an interesting feature. For these aspect ratios the system continuously

switches between two states: The length of the system here is either too long or too short to fit k intrinsic cell lengths, and the system tries to release this frustration by going towards a situation with one convection roll more or less. But the system cannot comfortably accommodate this state either, since at that moment there is no cluster at one of the sidewalls, and due to the extra dissipation with the wall the previous frustrated situation with an integer number of cells k is restored, repeating the series of events indefinitely. Only for a very small aspect ratio of L/d we observed a stable state with $k = 1/2$, i.e. one convection roll with one cluster. The aspect ratio here is too small to allow for any switching to a neighboring state, so this specific situation is stabilized.

The influence of the other two parameters, the shaking parameter S and the number of layers F , will be presented after the introduction of the numerical simulations in Sect. 3 and the theoretical stability analysis in Sect. 4.

3 Molecular dynamics simulations

In order to investigate information not available in experiment, we have also performed molecular dynamics (MD) simulations, using a granular dynamics code [68,69] to numerically study the shaken quasi 2D granular material. In such a model all the forces between the particles that are in contact with each other (or with the wall) are known, and also the positions and velocities of the particles, so the MD code calculates the particle trajectories from Newton’s equations of motion:

$$m \frac{d^2 \mathbf{r}_i}{dt^2} = \mathbf{f}_i + m \mathbf{g} \quad \text{for the translational motion,} \quad (2)$$

$$I_i \frac{d\boldsymbol{\omega}_i}{dt} = \mathbf{q}_i \quad \text{for the rotational motion,} \quad (3)$$

with \mathbf{r}_i the position of particle i , $\mathbf{f}_i = \sum \mathbf{f}_i$ the total force on particle i , \mathbf{g} the gravitational acceleration, I_i the moment of inertia, $\boldsymbol{\omega}_i = d\boldsymbol{\varphi}_i/dt$ the angular velocity, and \mathbf{q}_i the total torque on the particle. The inelastic particle–particle interaction is modelled by a 3-D soft sphere collision model, including tangential friction [68,69]. The coefficient of restitution e is incorporated in this soft sphere model following Eq. (27) of Deen et al. [69], and the restitution coefficient effectively also takes care of the damping in the model. The particle–wall interaction is modelled in the same way the particle–particle interaction is handled, so the wall is treated as a particle only now with infinite mass and radius.

In our simulations we have used the same parameters and dimensions as in the equivalent experiment: The container is filled with $N_p = L/d \times D/d \times F$ identical spherical particles, i.e., the number which corresponds to the filling height F . The coefficient of restitution e and friction coefficient for the particle–particle and particle–wall interactions determine the

total energy dissipation in the system. Note that due to the interaction with the wall the aspect ratio of the cell matters and we pick the same as in the experiments.

The friction coefficient is set to 0.03, while the coefficient of normal restitution (which for simplicity is assumed to be velocity-independent) is fitted to correctly describe the experimentally found onset for the case of $F = 10$ layers, yielding the very realistic values of $e = 0.957$ for steel and $e = 0.905$ for glass beads for both particle-particle and particle-wall interactions².

The numerical results for $S_c(F)$ are shown in Fig. 9, too, and they well agree with the experimental results within numerical and experimental precision. Snapshots from the numerical simulations are shown in Figs. 3 and 1, together with the corresponding experiments, again showing a one-to-one correspondence.

4 Theoretical model

In this section we are going to explain the experimental and numerical results by a hydrodynamic theory. Our model is analogous to the one used to determine the onset of Rayleigh-Bénard convection in classical fluids in which linear stability analysis is applied to the homogeneous base state [22,32]. We perform basically the same procedure with a more intricate base state, namely the inhomogeneous Leidenfrost state with the dense cluster on top of the gaseous region, and with various empirical constitutive relations due to the granular nature of the problem.

We will show that the linear stability analysis is able to precisely reproduce the critical shaking strength for which the onset of convection is observed in experiment. Moreover, we will show that the theoretically determined cell length $\Lambda(S, F, \varepsilon)$ reasonably agrees with the experimental observations.

4.1 Granular hydrodynamics

The basis of our analysis is formed by the hydrodynamic equations, which describe the three hydrodynamic continuum fields: The number density $n(x, y, t)$, the velocity field $\mathbf{u}(x, y, t)$, and the temperature $T(x, y, t)$ [32]. Our setup is quasi 2D so we restrict the analysis to two spatial directions (x, y) , which can obviously be generalized to 3D as well. Here we present an essential model that includes all the elemental features necessary to capture the phenomena observed.

The first continuum field, the density, is described by the continuity equation (or mass balance) and describes how the density varies in time:

$$\frac{\partial n}{\partial t} + \mathbf{u} \cdot \nabla n + n \nabla \cdot \mathbf{u} = 0. \quad (4)$$

Secondly, the time-variations of the components of the two-dimensional velocity field \mathbf{u} are governed by the Navier-Stokes equation (i.e. the momentum or force balance):

$$mn \left(\frac{\partial \mathbf{u}}{\partial t} + \mathbf{u} \cdot \nabla \mathbf{u} \right) = mng - \nabla p + \nabla \cdot \left(\mu \left[\nabla \mathbf{u} + (\nabla \mathbf{u})^T \right] \right) + \nabla (\lambda \nabla \cdot \mathbf{u}), \quad (5)$$

in which m is the mass of a single particle, p the pressure, \mathbf{g} the gravitational acceleration, μ the shear viscosity and λ the second viscosity. The velocity field \mathbf{u} is a vector in two dimensions, so Eq. (5) actually represents two equations:

$$mn \left[\frac{\partial u_x}{\partial t} + \left(u_x \frac{\partial u_x}{\partial x} + u_y \frac{\partial u_x}{\partial y} \right) \right] = - \frac{\partial p}{\partial x} + 2 \frac{\partial}{\partial x} \left(\mu \frac{\partial u_x}{\partial x} \right) + \frac{\partial}{\partial y} \left[\mu \left(\frac{\partial u_x}{\partial y} + \frac{\partial u_y}{\partial x} \right) \right] + \frac{\partial}{\partial x} \left[\lambda \left(\frac{\partial u_x}{\partial x} + \frac{\partial u_y}{\partial y} \right) \right], \quad (6)$$

$$mn \left[\frac{\partial u_y}{\partial t} + \left(u_x \frac{\partial u_y}{\partial x} + u_y \frac{\partial u_y}{\partial y} \right) \right] = - mng - \frac{\partial p}{\partial y} + 2 \frac{\partial}{\partial y} \left(\mu \frac{\partial u_y}{\partial y} \right) + \frac{\partial}{\partial x} \left[\mu \left(\frac{\partial u_x}{\partial y} + \frac{\partial u_y}{\partial x} \right) \right] + \frac{\partial}{\partial y} \left[\lambda \left(\frac{\partial u_x}{\partial x} + \frac{\partial u_y}{\partial y} \right) \right]. \quad (7)$$

The third continuum field is the granular temperature, which is defined as the velocity fluctuations of the particles around the mean velocity, i.e. $\frac{1}{2}k_B T = \frac{1}{2}m (\langle \mathbf{u}^2 \rangle - \langle \mathbf{u} \rangle^2)$ with $k_B = 1$. The temperature change in time is described by the energy equation or energy balance:

$$n \frac{\partial T}{\partial t} + n \mathbf{u} \cdot \nabla T = \nabla \cdot (\kappa \nabla T) - p (\nabla \cdot \mathbf{u}) - I, \quad (8)$$

where κ is the thermal conductivity and I is the dissipative term due to the inelastic particle collisions. In Eq. (8) we neglected terms which are quadratic in $\nabla \mathbf{u}$.

4.2 Constitutive relations

The granular hydrodynamic equations (4)–(8) are to be complemented by constitutive relations for the pressure field p , the energy dissipation rate I , and the transport coefficients κ , μ , and λ . Since our system combines dilute, gaseous regions with clusters where the density approaches the closed packed value, we need to take excluded volume effects into account.

² Note that higher values for e are obtained when a higher friction coefficient is used, reflecting that the total energy dissipation in the system must stay constant.

First we have the equation of state for a two dimensional granular fluid [28,70,71]:

$$p = nT \frac{n_c + n}{n_c - n}, \quad \text{with } n_c = \frac{2}{\sqrt{3}d^2}, \tag{9}$$

which is the ideal gas law with a VanderWaals-like correction [70] to account for the excluded area. Here $n_c = 2/\sqrt{3}d^2$ the number density of a hexagonal close-packed crystal.

The second constitutive relation concerns the energy dissipation rate I [28,70,71]:

$$I = \frac{\varepsilon}{\gamma_c \ell} nT \sqrt{\frac{T}{m}}. \tag{10}$$

Here the inelasticity parameter $\varepsilon = (1 - e^2)$, which we already identified as one of the experimental control parameters of this system, shows up also in the theoretical model. The value for the constant $\gamma_c = 2.26$ has been adopted from [70] in the same spirit as above.

The first transport coefficient is the thermal conductivity κ [28,70,71]:

$$\kappa = \frac{n(\alpha \ell + d)^2}{\ell} \sqrt{\frac{T}{m}}, \tag{11}$$

with the mean free path being given by $\ell = (n_c - n)/[\sqrt{8}nd(n_c - an)]$ following [70], with the constant $a = 1 - \sqrt{3/8} = 0.39$ and n_c the number density of a hexagonal close-packed crystal. For the constant α we adopted the value $\alpha = 0.6$ from [71].

In the literature various choices have been proposed for the shear viscosity μ in granular systems [55,59,72–74], and as it turns out it is quite critical which one we take. In Appendix A we will show that the results for our system strongly depend on the relation chosen for μ by using some of the available relations. We find good agreement with experiment when we take:

$$\mu = mPr \kappa, \tag{12}$$

in which Pr is the Prandtl number, which measures the ratio between diffusive momentum and energy transfer. This dimensionless number is in principle unknown and we will show that in our system a constant Pr of order unity is consistent with our results, just as it is for molecular gases. Because the viscosity μ for our granular system behaves so analogously to classical fluids, we use the Stokes approximation (strictly speaking only applicable for incompressible fluids, for which the bulk viscosity is zero) to get the simplest expression for the second viscosity λ :

$$\lambda = -\frac{2}{3}\mu, \tag{13}$$

even though our gas is compressible.

4.3 Linearization around the Leidenfrost state

The model presented above is an extension of the one used in [28]. The Leidenfrost state $n_L(y)$, $T_L(y)$ is obtained numerically as described in that paper. We proceed to linearize (4), (6), (7), and (8) around this state by adding a small perturbation,

$$n(x, y, t) = n_L(y) + \delta n(x, y, t), \tag{14}$$

$$u_x(x, y, t) = 0 + \delta u_x(x, y, t), \tag{15}$$

$$u_y(x, y, t) = 0 + \delta u_y(x, y, t), \tag{16}$$

$$T(x, y, t) = T_L(y) + \delta T(x, y, t). \tag{17}$$

This perturbed Leidenfrost state is inserted in the four hydrodynamic equations (4), (6), (7), and (8). We leave this as an exercise to the reader.

4.4 Boundary conditions

The linearized hydrodynamic equations are accompanied by boundary conditions for the perturbed density, velocities, and temperature. First, conservation of particles must apply. Since the Leidenfrost density obeys $\int_0^L dx \int_0^\infty dy n_L(y) = N_{\text{total}} = Fn_c d^2$, the integral over the perturbed number density must vanish,

$$\int_0^L dx \int_0^\infty dy \delta n(x, y, t) = 0. \tag{18}$$

Here the number of layers F (already identified as a control parameter in the experiments) arises as a relevant control parameter also in the theoretical model. As we will see later, this conservation condition (18) will not be used directly in the mathematical solution of the model, but still reflects an essential feature of the system.

We assume that the velocity field in the x -direction has an extremum (either a maximum or a minimum) at the bottom of the container, so the derivative of δu_x should be zero here:

$$\left. \frac{\partial(\delta u_x)}{\partial y} \right|_{y=0} = 0. \tag{19}$$

The velocity component in the y -direction necessarily vanishes at the bottom, and consequently

$$\delta u_y(x, 0, t) = 0. \tag{20}$$

For the boundary conditions at the top ($y \rightarrow \infty$) we assume that the velocity field vanishes altogether, leading to the following relations for the perturbed velocity fields:

$$\lim_{y \rightarrow \infty} \delta u_x(x, y, t) = 0, \tag{21}$$

$$\lim_{y \rightarrow \infty} \delta u_y(x, y, t) = 0. \tag{22}$$

As we impose a granular temperature T_0 at the bottom [with $T_0 \propto m(af)^2$ directly related to the kinetic energy imparted to the particles by the vibrating bottom], the boundary condition for the perturbed temperature should be zero:

$$\delta T(x, 0, t) = 0. \tag{23}$$

Finally we have the boundary condition for the granular temperature at the top, which we assume to vanish just like the velocity field, which stands to reason, since $T(x, y, t)$ represents the velocity fluctuations. So, the condition for perturbed temperature at the top becomes

$$\lim_{y \rightarrow \infty} \delta T(x, y, t) = 0. \tag{24}$$

As will be seen in Sect. 4.6, these seven boundary conditions are sufficient to solve the system of equations.

4.5 Non-dimensionalizing the hydrodynamic equations

The next step is to non-dimensionalize our linearized hydrodynamic equations and boundary conditions. To this end we first have to choose non-dimensional units. First, the density is made dimensionless by the number density n_c of a hexagonal close packing in 2D:

$$n \mapsto \tilde{n} = \frac{n}{n_c}, \quad \text{with } n_c = \frac{2}{\sqrt{3}d^2}. \tag{25}$$

Secondly, the temperature field is made dimensionless by the imposed granular temperature at the bottom:

$$T \mapsto \tilde{T} = \frac{T}{T_0}. \tag{26}$$

For the dimensionless length scales in our system we can choose between the container length L and the particle diameter d . Since the latter one is kept constant throughout our study, and the first one not, we non-dimensionalize the length scales as follows:

$$x \mapsto \tilde{x} = \frac{x}{d}, \tag{27}$$

$$y \mapsto \tilde{y} = \frac{y}{d}, \tag{28}$$

and we do the same for the mean free path

$$\begin{aligned} \ell &= \frac{1}{\sqrt{8}nd} \frac{n_c - n}{n_c - an} \mapsto \tilde{\ell} = \frac{\ell}{d} \\ &= \sqrt{\frac{3}{32}} \left[\frac{1}{\tilde{n}} \left(\frac{1 - \tilde{n}}{1 - a\tilde{n}} \right) \right], \end{aligned} \tag{29}$$

with $a = 1 - \sqrt{3/8}$ [70].

To make the time t dimensionless we make use of the dimensionality of the granular temperature (energy), the mass of one particle m , and the diameter d :

$$t \mapsto \tilde{t} = t \frac{\sqrt{T_0/m}}{d}, \tag{30}$$

and consequently the velocity fields u_x and u_y become in dimensionless form:

$$u_x \mapsto \tilde{u}_x = \frac{u_x}{\sqrt{T_0/m}}, \tag{31}$$

$$u_y \mapsto \tilde{u}_y = \frac{u_y}{\sqrt{T_0/m}}. \tag{32}$$

By inserting the dimensionless fields into the hydrodynamic equations we deduce the non-dimensional form of p , I , and the transport coefficients of (9)–(13). The equation of state then becomes:

$$\tilde{p} = \frac{p}{n_c T_0} = \tilde{n} \tilde{T} \frac{1 + \tilde{n}}{1 - \tilde{n}}. \tag{33}$$

The dimensionless form of the energy dissipation rate I is:

$$\tilde{I} = \frac{Id}{n_c T_0 \sqrt{T_0/m}} = \frac{\varepsilon}{\gamma} \frac{\tilde{n} \tilde{T} \sqrt{\tilde{T}}}{\tilde{\ell}}. \tag{34}$$

The transport coefficient κ reads in dimensionless form

$$\begin{aligned} \kappa &= \frac{n(\alpha\ell + d)^2}{\ell} \sqrt{\frac{T}{m}} \mapsto \tilde{\kappa} = \frac{\kappa}{n_c d \sqrt{T_0/m}} \\ &= \frac{(\alpha\tilde{\ell} + 1)^2}{\tilde{\ell}} \tilde{n} \sqrt{\tilde{T}}. \end{aligned} \tag{35}$$

Equation (12) relates the shear viscosity μ to the thermal conductivity κ , so μ now reads in dimensionless form:

$$\tilde{\mu} = \text{Pr} \tilde{\kappa}, \tag{36}$$

and from (13) the second viscosity λ follows immediately:

$$\tilde{\lambda} = -\frac{2}{3} \text{Pr} \tilde{\kappa}. \tag{37}$$

We can now write the hydrodynamic equations in dimensionless form. For every equation we have sorted the terms up to $O(\delta^2)$ in the following way: $\delta\tilde{n}$, $\delta\tilde{u}_x$, $\delta\tilde{u}_y$, and $\delta\tilde{T}$, each on its own line, this reflects the fact that the total perturbation is a four-vector with these four components. The structure of the problem (and of its solution) becomes much more transparent if we adhere to this vectorial notation. The linearized continuity equation becomes in dimensionless form:

$$\frac{\partial(\delta\tilde{n})}{\partial\tilde{t}} = 0 - \tilde{n}_L \frac{\partial(\delta\tilde{u}_x)}{\partial\tilde{x}} - \frac{\partial\tilde{n}_L}{\partial\tilde{y}} \delta\tilde{u}_y - \tilde{n}_L \frac{\partial(\delta\tilde{u}_y)}{\partial\tilde{y}} + 0. \tag{38}$$

The dimensionless form of the force balance in the x -direction becomes:

$$\begin{aligned} \tilde{n}_L \frac{\partial(\delta\tilde{u}_x)}{\partial\tilde{t}} &= -\frac{\partial\tilde{p}}{\partial\tilde{n}} \Big|_L \frac{\partial(\delta\tilde{n})}{\partial\tilde{x}} + 2\tilde{\mu}_L \frac{\partial^2(\delta\tilde{u}_x)}{\partial\tilde{x}^2} \\ &+ \frac{\partial}{\partial\tilde{y}} \left[\tilde{\mu}_L \frac{\partial(\delta\tilde{u}_x)}{\partial\tilde{y}} \right] + \tilde{\lambda}_L \frac{\partial^2(\delta\tilde{u}_x)}{\partial\tilde{x}^2} \\ &+ \frac{\partial}{\partial\tilde{y}} \left[\tilde{\mu}_L \frac{\partial(\delta\tilde{u}_y)}{\partial\tilde{x}} \right] + \tilde{\lambda}_L \frac{\partial^2(\delta\tilde{u}_y)}{\partial\tilde{x}\partial\tilde{y}} \\ &- \frac{\partial\tilde{p}}{\partial\tilde{T}} \Big|_L \frac{\partial(\delta\tilde{T})}{\partial\tilde{x}}. \end{aligned} \tag{39}$$

The force balance for the y -direction takes the following dimensionless form:

$$\begin{aligned} \tilde{n}_L \frac{\partial(\delta\tilde{u}_y)}{\partial\tilde{t}} = & -\frac{1}{S}\delta\tilde{n} - \frac{\partial}{\partial\tilde{y}} \left(\frac{\partial\tilde{p}}{\partial\tilde{n}} \Big|_L \right) \delta\tilde{n} - \frac{\partial\tilde{p}}{\partial\tilde{n}} \Big|_L \frac{\partial(\delta\tilde{n})}{\partial\tilde{y}} \\ & + \tilde{\mu}_L \frac{\partial^2(\delta\tilde{u}_x)}{\partial\tilde{x}\partial\tilde{y}} + \frac{\partial\tilde{\lambda}_L}{\partial\tilde{y}} \frac{\partial(\delta\tilde{u}_x)}{\partial\tilde{x}} + \tilde{\lambda}_L \frac{\partial^2(\delta\tilde{u}_x)}{\partial\tilde{x}\partial\tilde{y}} \\ & + 2\frac{\partial\tilde{\mu}_L}{\partial\tilde{y}} \frac{\partial(\delta\tilde{u}_y)}{\partial\tilde{y}} + 2\tilde{\mu}_L \frac{\partial^2(\delta\tilde{u}_y)}{\partial\tilde{y}^2} + \tilde{\mu}_L \frac{\partial^2(\delta\tilde{u}_x)}{\partial\tilde{x}^2} \\ & + \frac{\partial\tilde{\lambda}_L}{\partial\tilde{y}} \frac{\partial(\delta\tilde{u}_y)}{\partial\tilde{y}} + \tilde{\lambda}_L \frac{\partial^2(\delta\tilde{u}_y)}{\partial\tilde{y}^2} \\ & - \frac{\partial}{\partial\tilde{y}} \left(\frac{\partial\tilde{p}}{\partial\tilde{T}} \Big|_L \right) \delta\tilde{T} - \frac{\partial\tilde{p}}{\partial\tilde{T}} \Big|_L \frac{\partial(\delta\tilde{T})}{\partial\tilde{y}}. \end{aligned} \tag{40}$$

In the first term on the right hand side appears the dimensionless shaking strength S :

$$S = \frac{T_0}{mgd} \quad \text{with} \quad T_0 \propto m(af)^2. \tag{41}$$

This S was already introduced as the governing shaking parameter in the context of our experiments, see (1). Note that we did *not* use the more familiar dimensionless acceleration $\Gamma = a\omega^2/g$. This choice is now justified by hydrodynamic theory.

Finally, the energy balance in dimensionless form becomes:

$$\begin{aligned} \tilde{n}_L \frac{\partial(\delta\tilde{T})}{\partial\tilde{t}} = & \left[-\frac{\partial\tilde{I}}{\partial\tilde{n}} \Big|_L + \frac{\partial}{\partial\tilde{y}} \left(\frac{\partial\tilde{\kappa}}{\partial\tilde{n}} \Big|_L \right) \frac{\partial\tilde{T}_L}{\partial\tilde{y}} + \frac{\partial\tilde{\kappa}}{\partial\tilde{n}} \Big|_L \frac{\partial^2\tilde{T}_L}{\partial\tilde{y}^2} \right] \delta\tilde{n} \\ & + \frac{\partial\tilde{\kappa}}{\partial\tilde{n}} \Big|_L \frac{\partial\tilde{T}_L}{\partial\tilde{y}} \frac{\partial(\delta\tilde{n})}{\partial\tilde{y}} - \tilde{p}_L \frac{\partial(\delta\tilde{u}_x)}{\partial\tilde{x}} \\ & - \tilde{n}_L \frac{\partial\tilde{T}_L}{\partial\tilde{y}} \delta\tilde{u}_y - \tilde{p}_L \frac{\partial(\delta\tilde{u}_y)}{\partial\tilde{y}} \\ & + \left[\frac{\partial}{\partial\tilde{y}} \left(\frac{\partial\tilde{\kappa}}{\partial\tilde{T}} \Big|_L \right) \frac{\partial\tilde{T}_L}{\partial\tilde{y}} + \frac{\partial\tilde{\kappa}}{\partial\tilde{T}} \Big|_L \frac{\partial^2\tilde{T}_L}{\partial\tilde{y}^2} - \frac{\partial\tilde{I}}{\partial\tilde{T}} \Big|_L \right] \delta\tilde{T} \\ & + \left(\frac{\partial\tilde{\kappa}_L}{\partial\tilde{y}} + \frac{\partial\tilde{\kappa}}{\partial\tilde{T}} \Big|_L \frac{\partial\tilde{T}_L}{\partial\tilde{y}} \right) \frac{\partial(\delta\tilde{T})}{\partial\tilde{y}} + \tilde{\kappa}_L \frac{\partial^2(\delta\tilde{T})}{\partial\tilde{x}^2} \\ & + \tilde{\kappa}_L \frac{\partial^2(\delta\tilde{T})}{\partial\tilde{y}^2} \end{aligned} \tag{42}$$

The non-dimensionalization of the boundary conditions (18)–(24) is trivial.

4.6 Formulation of the eigenvalue problem

Having brought the linearized hydrodynamic equations plus the accompanying boundary conditions in dimensionless form, we now formulate the eigenvalue problem. In order to do so we apply the following Ansatz for the form of the

perturbations:

$$\delta\tilde{n} = N(\tilde{y})e^{ik_x\tilde{x}}e^{\gamma\tilde{t}}, \tag{43}$$

$$\delta\tilde{u}_x = U(\tilde{y})e^{ik_x\tilde{x}}e^{\gamma\tilde{t}}, \tag{44}$$

$$\delta\tilde{u}_y = V(\tilde{y})e^{ik_x\tilde{x}}e^{\gamma\tilde{t}}, \tag{45}$$

$$\delta\tilde{T} = \Theta(\tilde{y})e^{ik_x\tilde{x}}e^{\gamma\tilde{t}}. \tag{46}$$

Here $N(\tilde{y})$, $U(\tilde{y})$, $V(\tilde{y})$, and $\Theta(\tilde{y})$ are the vertical profiles of the perturbation fields. The terms with $e^{ik_x\tilde{x}}$ contain the wave number k_x , expressing the periodicity in the x -direction, see for example Fig. 1. This wavenumber is related to the natural wavelength Λ . As we will see later, the wavelength we observe in practice can deviate somewhat from this natural wavelength, because the wavelength has to be accommodated in the container length L . In the factor $e^{\gamma\tilde{t}}$ we have $\gamma = \gamma_R + i\gamma_I$, where the real part γ_R denotes the growth/decay rate of the perturbation and the imaginary part γ_I indicates the frequency of the wave, i.e., whether it is travelling wave or not. It turns out that the solution of our model does not show any travelling waves, meaning that $\gamma_I = 0$ and hence $\gamma = \gamma_R$. This matches the experimentally observed instabilities of the current study, which are found to be stationary. So when $\gamma < 0$ the Leidenfrost state is stable and when $\gamma > 0$ it is unstable. In the latter case the Leidenfrost state gives way to convection rolls for this specific value of γ , i.e. the *eigenvalue*, which we also called the growth rate of the perturbation.

This Ansatz is inserted in the four hydrodynamic equations, so the continuity equation (38) takes the form:

$$0 = \gamma N + \tilde{n}_L k_x U + \frac{\partial\tilde{n}_L}{\partial\tilde{y}} V + \tilde{n}_L V' + 0. \tag{47}$$

The force balance for the x -direction (39) transforms into:

$$\begin{aligned} 0 = & -\frac{\partial\tilde{p}}{\partial\tilde{n}} \Big|_L k_x N + \left[\tilde{n}_L \gamma + (2\tilde{\mu}_L + \tilde{\lambda}_L) k_x^2 \right] U - \frac{\partial\tilde{\mu}_L}{\partial\tilde{y}} U' \\ & - \tilde{\mu}_L U'' + \frac{\partial\tilde{\mu}_L}{\partial\tilde{y}} k_x V + (\tilde{\mu}_L + \tilde{\lambda}_L) k_x V' \\ & - \frac{\partial\tilde{p}}{\partial\tilde{T}} \Big|_L k_x \Theta, \end{aligned} \tag{48}$$

and the force balance for the y -direction (40) becomes:

$$\begin{aligned} 0 = & \left[\frac{1}{S} + \frac{\partial}{\partial\tilde{y}} \left(\frac{\partial\tilde{p}}{\partial\tilde{n}} \Big|_L \right) \right] N + \frac{\partial\tilde{p}}{\partial\tilde{n}} \Big|_L N' - \frac{\partial\tilde{\lambda}_L}{\partial\tilde{y}} k_x U \\ & - (\tilde{\mu}_L + \tilde{\lambda}_L) k_x U' + \left[\tilde{n}_L \gamma + \tilde{\mu}_L k_x^2 \right] V \\ & - \left[2\frac{\partial\tilde{\mu}_L}{\partial\tilde{y}} + \frac{\partial\tilde{\lambda}_L}{\partial\tilde{y}} \right] V' - [2\tilde{\mu}_L + \tilde{\lambda}_L] V'' \\ & + \frac{\partial}{\partial\tilde{y}} \left(\frac{\partial\tilde{p}}{\partial\tilde{T}} \Big|_L \right) \Theta + \frac{\partial\tilde{p}}{\partial\tilde{T}} \Big|_L \Theta'. \end{aligned} \tag{49}$$

Finally, the energy balance (42) takes the form:

$$\begin{aligned}
 0 = & \left[\frac{\partial \tilde{I}}{\partial \tilde{n}} \Big|_L - \frac{\partial}{\partial \tilde{y}} \left(\frac{\partial \tilde{\kappa}}{\partial \tilde{n}} \Big|_L \right) \frac{\partial \tilde{T}_L}{\partial \tilde{y}} - \frac{\partial \tilde{\kappa}}{\partial \tilde{n}} \Big|_L \frac{\partial^2 \tilde{T}_L}{\partial \tilde{y}^2} \right] N \\
 & - \frac{\partial \tilde{\kappa}}{\partial \tilde{n}} \Big|_L \frac{\partial \tilde{T}_L}{\partial \tilde{y}} N' + \tilde{p}_L k_x U + \tilde{n}_L \frac{\partial \tilde{T}_L}{\partial \tilde{y}} V + \tilde{p}_L V' \\
 & + \left[\tilde{n}_L \gamma - \tilde{\kappa}_L k_x^2 - \frac{\partial}{\partial \tilde{y}} \left(\frac{\partial \tilde{\kappa}}{\partial \tilde{T}} \Big|_L \right) \frac{\partial \tilde{T}_L}{\partial \tilde{y}} \right. \\
 & \left. - \frac{\partial \tilde{\kappa}}{\partial \tilde{T}} \Big|_L \frac{\partial^2 \tilde{T}_L}{\partial \tilde{y}^2} + \frac{\partial \tilde{I}}{\partial \tilde{T}} \Big|_L \right] \Theta \\
 & - \left[\frac{\partial \tilde{\kappa}}{\partial \tilde{y}} + \frac{\partial \tilde{\kappa}}{\partial \tilde{T}} \Big|_L \frac{\partial \tilde{T}_L}{\partial \tilde{y}} \right] \Theta' + \tilde{\kappa}_L \Theta'' . \tag{50}
 \end{aligned}$$

These four equations (47)–(50) can be written as a 4×4 matrix problem for the column vector (N, U, V, Θ) and its first and second derivative:

$$\mathbf{A} \cdot \frac{d^2}{d\tilde{y}^2} \begin{pmatrix} N \\ U \\ V \\ \Theta \end{pmatrix} + \mathbf{B} \cdot \frac{d}{d\tilde{y}} \begin{pmatrix} N \\ U \\ V \\ \Theta \end{pmatrix} + \mathbf{C} \cdot \begin{pmatrix} N \\ U \\ V \\ \Theta \end{pmatrix} = 0, \tag{51}$$

The elements of the 4×4 matrices **A**, **B**, and **C** can be read from the hydrodynamic equations (47)–(50):

$$\mathbf{A} = \begin{pmatrix} 0 & 0 & 0 & 0 \\ 0 & -\tilde{\mu}_L & 0 & 0 \\ 0 & 0 & -2\tilde{\mu}_L - \tilde{\lambda}_L & 0 \\ 0 & 0 & 0 & \tilde{\kappa}_L \end{pmatrix}, \tag{52}$$

$$\mathbf{B} = \begin{pmatrix} 0 & 0 & \tilde{n}_L & 0 \\ 0 & -\frac{\partial \tilde{\mu}_L}{\partial \tilde{y}} & (\tilde{\mu}_L + \tilde{\lambda}_L) k_x & 0 \\ \frac{\partial \tilde{p}}{\partial \tilde{n}} \Big|_L & -(\tilde{\mu}_L + \tilde{\lambda}_L) k_x & -2 \frac{\partial \tilde{\mu}_L}{\partial \tilde{y}} - \frac{\partial \tilde{\lambda}_L}{\partial \tilde{y}} & \frac{\partial \tilde{p}}{\partial \tilde{T}} \Big|_L \\ \frac{\partial \tilde{\kappa}}{\partial \tilde{n}} \Big|_L \frac{\partial \tilde{T}_L}{\partial \tilde{y}} & 0 & \tilde{p}_L & -\frac{\partial \tilde{\kappa}_L}{\partial \tilde{y}} - \frac{\partial \tilde{\kappa}}{\partial \tilde{T}} \Big|_L \frac{\partial \tilde{T}_L}{\partial \tilde{y}} \end{pmatrix}, \tag{53}$$

$$\mathbf{C} = \begin{pmatrix} \gamma & \tilde{n}_L k_x & ; \\ -\frac{\partial \tilde{p}}{\partial \tilde{n}} \Big|_L k_x & \tilde{n}_L \gamma + (2\tilde{\mu}_L + \tilde{\lambda}_L) k_x^2 & ; \\ \frac{1}{8} + \frac{\partial}{\partial \tilde{y}} \left(\frac{\partial \tilde{p}}{\partial \tilde{n}} \Big|_L \right) & -\frac{\partial \tilde{\lambda}_L}{\partial \tilde{y}} k_x & ; \\ -\frac{\partial}{\partial \tilde{y}} \left(\frac{\partial \tilde{\kappa}}{\partial \tilde{n}} \Big|_L \right) \frac{\partial \tilde{T}_L}{\partial \tilde{y}} & \tilde{p}_L k_x & ; \\ + \frac{\partial \tilde{I}}{\partial \tilde{n}} \Big|_L - \frac{\partial \tilde{\kappa}}{\partial \tilde{n}} \Big|_L \frac{\partial^2 \tilde{T}_L}{\partial \tilde{y}^2} & & \end{pmatrix} . \tag{54}$$

$$\begin{pmatrix} ; & \frac{\partial \tilde{n}_L}{\partial \tilde{y}} & 0 \\ ; & \frac{\partial \tilde{\mu}_L}{\partial \tilde{y}} k_x & -\frac{\partial \tilde{p}}{\partial \tilde{T}} \Big|_L k_x \\ ; & \tilde{n}_L \gamma + \tilde{\mu}_L k_x^2 & \frac{\partial}{\partial \tilde{y}} \left(\frac{\partial \tilde{p}}{\partial \tilde{T}} \Big|_L \right) \\ ; & \tilde{n}_L \frac{\partial \tilde{T}_L}{\partial \tilde{y}} & \tilde{n}_L \gamma - \frac{\partial}{\partial \tilde{y}} \left(\frac{\partial \tilde{\kappa}}{\partial \tilde{T}} \Big|_L \right) \frac{\partial \tilde{T}_L}{\partial \tilde{y}} \\ & & -\tilde{\kappa}_L k_x^2 - \frac{\partial \tilde{\kappa}}{\partial \tilde{T}} \Big|_L \frac{\partial^2 \tilde{T}_L}{\partial \tilde{y}^2} + \frac{\partial \tilde{I}}{\partial \tilde{T}} \Big|_L \end{pmatrix} .$$

The matrices **A**, **B** and **C** are functions of the height \tilde{y} and evidently all of them are evaluated at the unperturbed Leidenfrost state $(\tilde{n}_L(\tilde{y}), 0, 0, \tilde{T}_L(\tilde{y}))$. To calculate the matrices **A**, **B** and **C** one needs the constitutive relations and their various derivatives (pressure \tilde{p} , energy dissipation rate \tilde{I} , thermal

conductivity $\tilde{\kappa}$, shear viscosity $\tilde{\mu}$, and second viscosity $\tilde{\lambda}$). These are given in Appendix B.

Note that the first equation in (51) is of first order, whereas the other three are of second order, such that the seven boundary conditions from Sect. 4.4 completely determine the solution.

4.7 Linear stability analysis using spectral methods

To solve the eigenvalue problem (51), consisting of four coupled ordinary differential equations, standard methods for linear equations can be applied.

The goal is to locate the onset of convection by finding the eigenvalue γ for which the Leidenfrost state becomes unstable (i.e. $\gamma > 0$). The wave number k_x corresponding to the most unstable mode (maximal γ -value) determines the dominant perturbation that will start the convection for this particular Leidenfrost state.

We use the spectral-collocation method to perform the linear stability analysis. Spectral methods find their origin in the 1940s and were revived by Orszag [75] in the 1970s, after which they became mainstream in scientific computation [76]. These methods are designed to solve differential equations, making use of trial functions (also known as expansion or approximating functions) and the so-called test or weight functions.

The trial functions represent the approximate solution of the differential equations. They are linear combinations of a suitable family of basis functions, e.g. trigonometric (Fourier) polynomials; these functions are global in contrast to the basis functions used for instance in finite-element or finite-difference methods, which are local. The test functions guarantee that the differential equations and the boundary conditions are satisfied at the collocation points.

Thanks to the linearity of the problem we have various options for the trial basis functions, namely trigonometric or Fourier polynomials, Chebyshev polynomials, Legendre polynomials, and many more. In the y -direction our system of equations is non-periodic, so Fourier polynomials are not suitable as trial basis functions along the y -direction. Chebyshev polynomials are the next candidate [76] and have proven to be successful in performing a linear stability analysis in granular studies by Alam and Nott [21,23] in Couette flow and Forterre and Pouliquen [22] in chute flow. So it is natural to adopt this method also in our case and indeed, it turns out to be convenient for our current stability analysis of the Leidenfrost state. The Chebyshev polynomials $T_k(y)$ are defined as follows on the $y = [-1, 1]$ Chebyshev domain [76]:

$$T_k(y) = \cos(k \cos^{-1} y), \quad k = 0, 1, 2, \dots \tag{55}$$

A particular convenient choice for the collocation points y_j in the case of Chebyshev polynomials is the Gauss-Lobatto

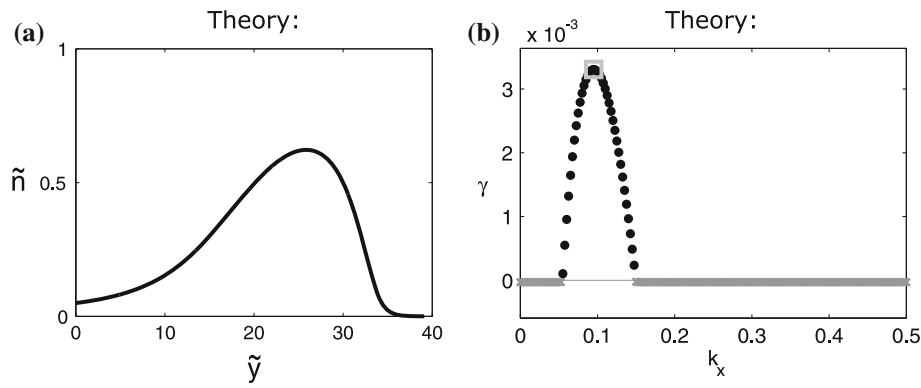


Fig. 5 *Theory*: **a** The density profile $\tilde{n}(\tilde{y})$ for the Leidenfrost state for $F = 11$ layers and shaking strength $S = 200$, used as a base state for the linear stability analysis. **b** The growth rate γ as a function of the wave number k_x for the Leidenfrost solution depicted in **a**. For all grey crosses $\gamma < 0$, meaning that the Leidenfrost state is stable. The black

dots indicate the unstable modes corresponding to $\gamma > 0$. The most unstable mode, marked by the *grey square*, defines the dominant wave number ($k_{x,max} = 0.095$) and hence the length of the convection cell: $\Lambda = 2\pi/k_{x,max} = 66$ particle diameters

choice, which fixes the trial functions at the points:

$$y_j = \cos\left(\frac{\pi j}{N}\right), \quad j = 0, \dots, N, \tag{56}$$

and this transforms the basis functions into:

$$T_k(y_j) = \cos\left(\frac{\pi j k}{N}\right), \quad j = 0, \dots, N, \quad k = 0, 1, 2, \dots \tag{57}$$

The Gauss-Lobatto points (56) are used to collocate the momentum and energy equations plus the corresponding boundary conditions. Note that the number of collocation points N controls the number of spurious modes that appear due to the discretization. We found that $N = 50$ is sufficient to prevent spurious eigenvalues and to determine the physical modes with high accuracy.

It is important to stress that in order to retrieve a correct solution, a correct and high resolution base state, i.e., Leidenfrost state, should be used. For (incorrect or unresolved) base states the linear stability analysis results in spurious traveling wave solutions with $\gamma_I \neq 0$, so the imaginary part of the growth rate becomes nonzero.

To collocate the continuity equation we use the so-called Gauss points:

$$y_j = \cos\left(\pi \frac{(2j + 1)}{2N + 2}\right), \quad j = 0, \dots, N, \tag{58}$$

which brings the corresponding basis functions into the following form:

$$T_k(y_j) = \cos\left(\frac{\pi(2j + 1)k}{2N + 2}\right), \quad j = 0, \dots, N, \quad k = 0, 1, 2, \dots \tag{59}$$

In the way the Gauss and Gauss-Lobatto points (56, 58) are defined one sees the advantage of the Chebyshev spec-

tral collocation method: The boundary regions, which are most relevant in this stability problem, are covered with high resolution.

One may note that the Gauss points do not include the boundary points, whereas the Gauss-Lobatto points *do* describe the boundaries. The reason for this is that we do not want to collocate the density at the boundary, because we do not have actual boundary conditions for $\delta\tilde{n}$. [Instead for $\delta\tilde{n}$ we have the integral constraint of the particle conservation over the whole system (18).] This is no problem, since we can reduce the set of four hydrodynamic equations through elimination of the number density $\delta\tilde{n}$ by making use of the continuity equation, which is of first order, as already remarked in the context of (51). We then get a system of three coupled equations for the velocity fields $\delta\tilde{u}_x$ and $\delta\tilde{u}_y$, and the granular temperature $\delta\tilde{T}$. Therefore we do not need a boundary condition for $\delta\tilde{n}^3$, but only boundary conditions (at the bottom and the top) for $\delta\tilde{u}_x$, $\delta\tilde{u}_y$, and $\delta\tilde{T}$, i.e. the conditions (19)–(24).

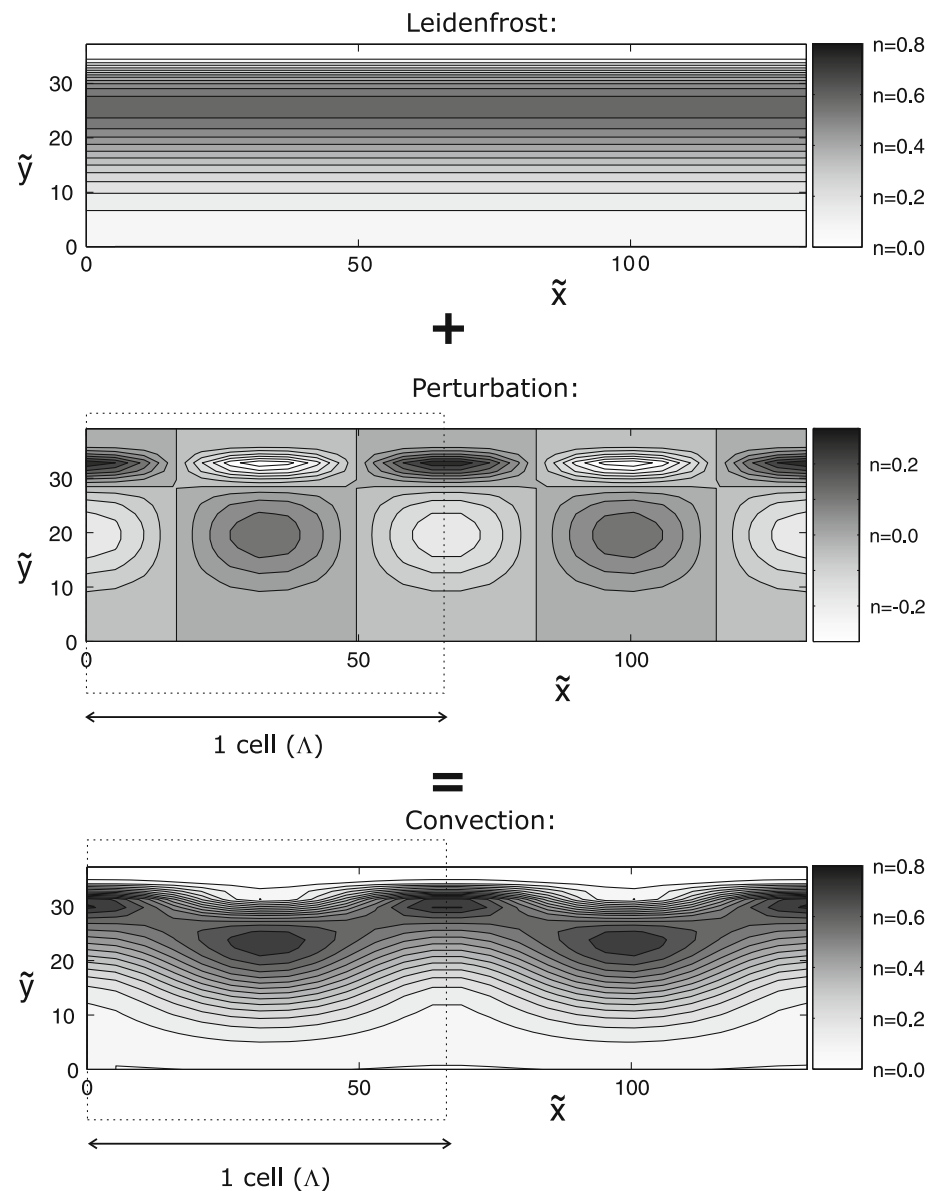
The matrix problem defined by (51)–(54) and the boundary conditions of (19)–(24) are then translated from the physical domain $\tilde{y} = [0, H_{max}]$ (with H_{max} the truncated height of the system in particle diameters) to the $y = [-1, 1]$ Chebyshev domain (on which the trial functions are defined) via the following transformation:

$$y = \lim_{H \rightarrow H_{max}} \frac{2\tilde{y}}{H} - 1. \tag{60}$$

We have used a truncated physical domain up to $y = H_{max}$ where we have also applied the boundary conditions. The value of H_{max} ranges from 30 to 80 particle diameters

³ One can also collocate the continuity equation at Gauss-Lobatto points, but that calls for using artificial boundary conditions for the density field that may lead to one spurious eigenvalue [21].

Fig. 6 *Theory*: The construction of the density profile of the convective state for $F = 11$ and $S = 200$ by adding the perturbation (obtained from the linear stability analysis taken over one natural time unit $\tilde{t} = 1/\gamma$, see text) to the corresponding Leidenfrost state. From the stability analysis of Fig. 5 we know that the cell length is $\Lambda = 66$ particle diameters; two cell lengths are depicted here. *Dark colors* indicate regions of high density



depending on the parameters. Using the grid formed by the Gauss and Gauss-Lobatto points the linear stability analysis of the hydrodynamic model is performed using the spectral-collocation method, which has the advantage that the derivatives are easily computed and that the boundary conditions are dealt with in a relatively simple way [76].

4.8 Solution

As an example of a state on which we have performed the stability analysis, in Fig. 5a we show the Leidenfrost state for $F = 11$ layers at a shaking strength $S = 200$. Since this base state is a numerical solution, the matrices **A**, **B**, and **C** necessary to solve (51) are generated numerically. The growth

rate γ obtained from the solution of (51), using the spectral-collocation method, is depicted in Fig. 5b. It shows an interval of k_x -values for which γ is positive (i.e. the Leidenfrost state is unstable). The convection mode that will manifest itself for this particular Leidenfrost state is associated with the wave number $k_{x,\max} = 0.095$, for which the growth rate is maximal (marked by the grey square). Thus, hydrodynamic theory predicts a cell length (consisting of a pair of counter-rotating convection rolls) of $\Lambda = 2\pi/k_{x,\max} = 66$ particle diameters.

From this dominant perturbation mode we can determine the density profile of the corresponding convection pattern as illustrated in Fig. 6: It is the sum of the Leidenfrost density profile and the perturbation profile. In this figure we have taken the perturbation over

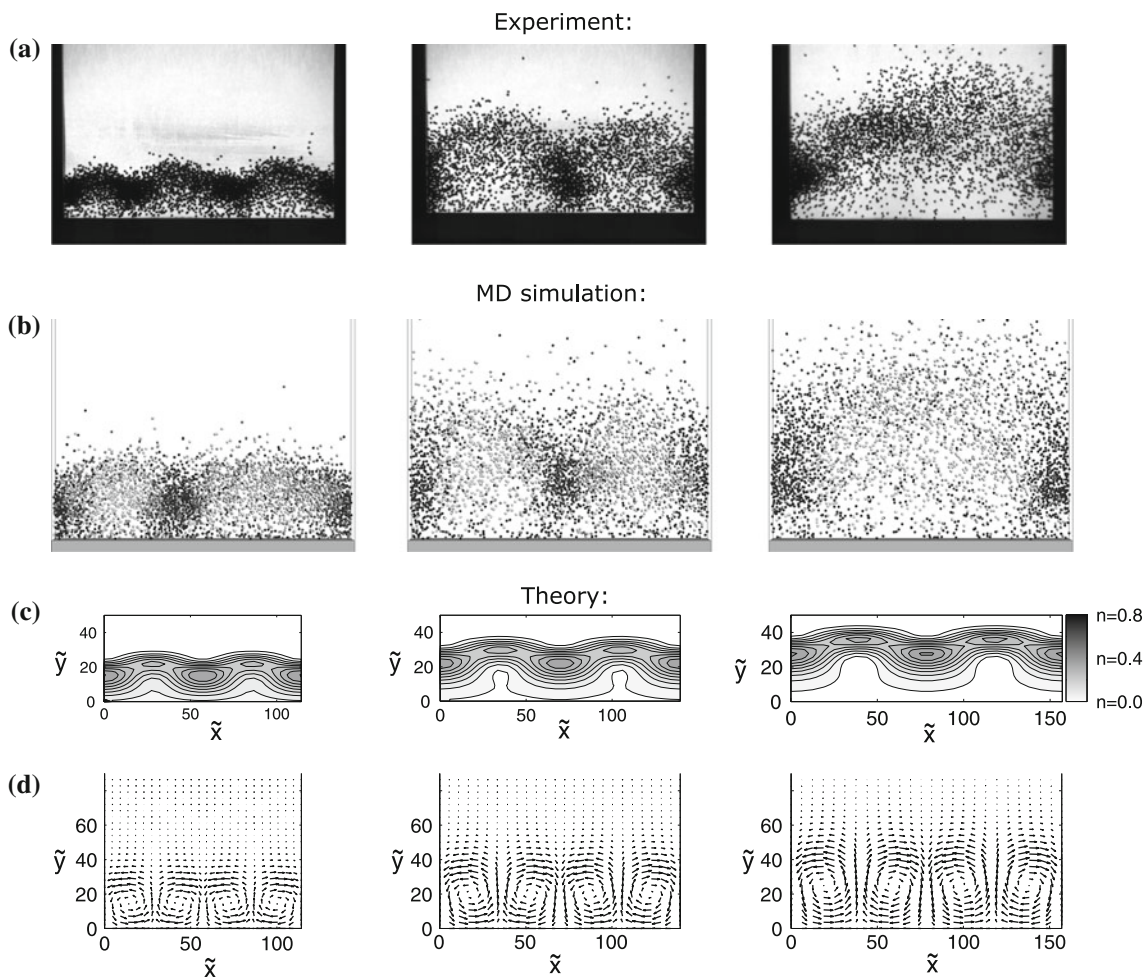


Fig. 7 Experiment, MD simulation, and theory: **a** Convection patterns for $F = 6.2$ particle layers in a container of length $L/d = 101$ at three consecutive shaking strengths: $S = 58$, $S = 130$, and $S = 202$. Available as movie 4 with the online version of the paper. **b** Snapshots of MD simulations that are completely equivalent to the experiments

shown above, so $F = 6.2$ layers in a container of length $L/d = 101$ for $S = 58$, $S = 130$, and $S = 202$. Available as movie 4 with the online version of the paper. **c, d** Two cell lengths ($2\Lambda/d$) of the theoretical density and velocity profiles for $F = 6$ layers shaken at $S = 60$, $S = 130$, and $S = 200$. The respective cell lengths are $\Lambda/d = 57, 70$, and 79

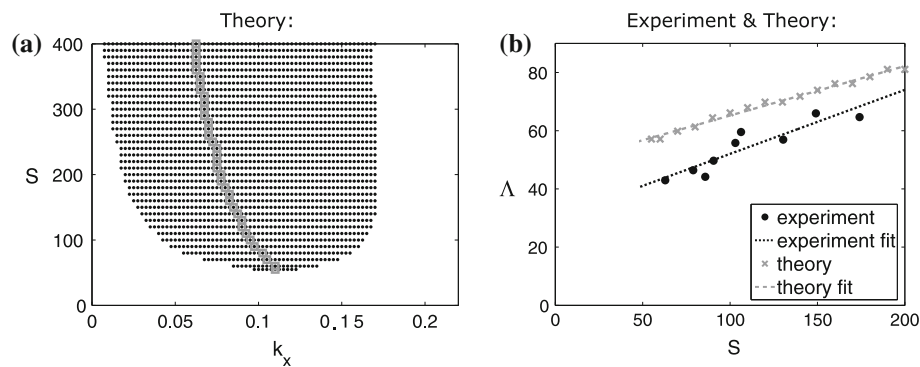


Fig. 8 **a** Shaking strength S versus wave number k_x for $F = 6$ layers. The black dots correspond to the unstable modes k_x as determined by the linear stability analysis of our hydrodynamic model. The smallest S -value for which an unstable mode is found defines the onset of convection: $S_{conv} = 55$. The grey squares mark the most unstable mode at each shaking strength and determines the theoretical length of a convective cell: $\Lambda = 2\pi/k_{x,max}$. **b** Experiment versus theory: Cell length

Λ as a function of shaking strength S . The black dots indicate the experiments with $F = 6.2$ particle layers, where Λ is determined from a plot such as depicted in Fig. 4e. The dotted black line is a linear fit through the experimental data. The grey crosses are theoretical data obtained from the instability region depicted in **a**, and the dashed grey line is a linear fit through these theoretical points

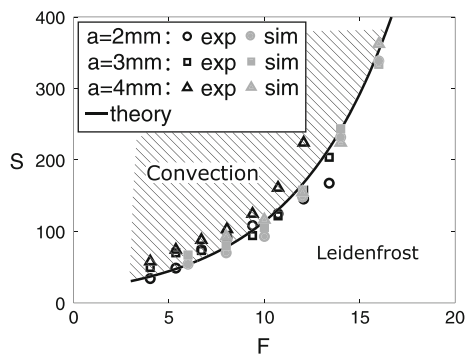


Fig. 9 Experiment, MD simulation, and theory: The convection threshold in (S, F) -phase diagram. The experiments and simulations are performed with $d = 1$ mm glass beads, with shaking amplitude $a = 2.0$ mm (dots), $a = 3.0$ mm (squares), and $a = 4.0$ mm (triangles). The shaking strength S is varied via the frequency f . The open black symbols correspond to the experiments and the solid grey ones to the MD simulations. The theoretical line (black) is a fit through the theoretical data points (not shown), which depend sensitively on the expression used for the viscosity: Here we have taken $\tilde{\mu}(\tilde{n}, \tilde{T}) = \text{Pr} \tilde{\kappa}(\tilde{n}, \tilde{T})$ with the dimensionless Prandtl number $\text{Pr} = 1.7$ as the only fit parameter in the system. An experiment and simulation are available as movie 5 with the online version of the paper

one natural time unit for the growth rate γ , i.e., we used $\tilde{t} = 1/\gamma$ in $\tilde{n}_L(\tilde{y}) + N(\tilde{y})e^{ik_x \tilde{x}} e^{\gamma \tilde{t}}$ to match the observed patterns.

This linear stability analysis has been performed on a large number of Leidenfrost states obtained from the hydrodynamic model, where we systematically varied the number of layers F and the shaking strength S . This ultimately leads to the phase diagram of Fig. 9 in which we compare hydrodynamic theory with the experimental observations, as will be discussed in detail in the next section.

5 Comparing experiment, numerics, and theory

Now that we have passed the onset of convection we get into the region of fully developed convection, so how do the rolls look like when considering the density-, velocity-, and granular temperature field? In this section we will compare the results of the experiments, molecular dynamics simulations, and theory.

5.1 Cell length Λ versus shaking strength S

The comparison of experiment, MD simulation, and theory of Fig. 7 reveals that if the shaking strength S is increased the convective cells expand and consequently the number of convection rolls fitting the container becomes smaller. This dependence is studied in more detail in Fig. 8 for the experiments and hydrodynamic theory.

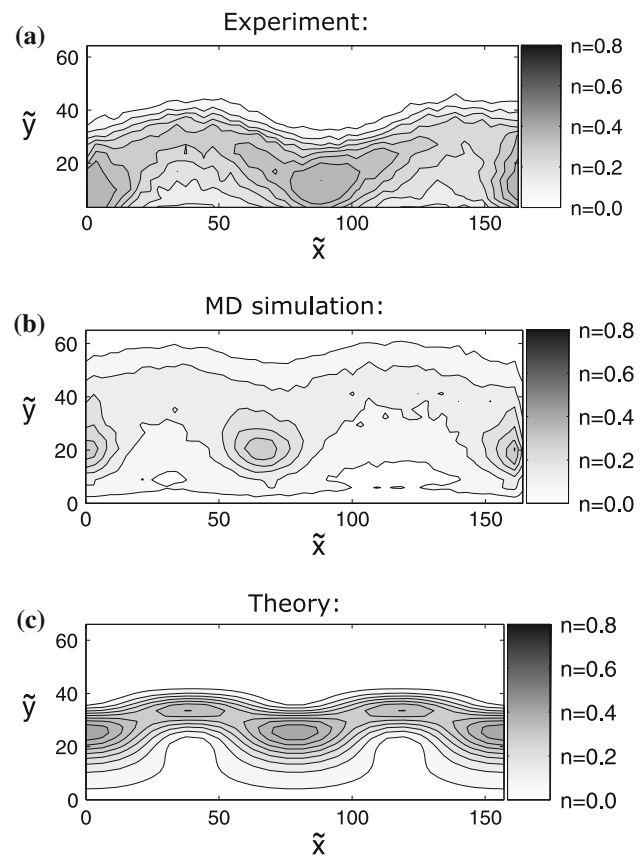


Fig. 10 Comparing experiment, MD simulation, and theory: **a** The density profile (averaged over 250 high-speed snapshots) of $F = 6.2$ layers of steel beads in a container of length $L/d = 164$, shaken at $a = 4.0$ mm and $f = 52$ Hz ($S = 174$). This experimental profile shows 2 convective cells, where the color coding indicates the regions with high density (black) and low density (white). **b** Averaged density profile of a MD simulation showing two convective cells for $F = 6.2$ layers in a container of length $L/d = 164$, with shaking amplitude $a = 4.0$ mm and frequency $f = 52$ Hz ($S = 174$), as in the experiment shown in **a**. **c** The theoretical density profile for $F = 6$ and $S = 170$ plotted for two cell lengths: $2\Lambda/d = 158$

Figure 8a shows which Leidenfrost states for $F = 6$ layers are stable (corresponding to an eigenvalue $\gamma < 0$, white region), and which ones are unstable ($\gamma > 0$, dotted region) and thus give way to convection. The region of instability defines the critical shaking strength $S_{\text{conv}} = 55$ required for the onset of convection for this number of layers F . When the shaking strength is increased beyond this critical value, the instability region is seen to widen and at the same time the dominant wave number $k_{x,\text{max}}$ (marked by the grey squares in Fig. 8a) becomes smaller. This means that the cell length $\Lambda = 2\pi/k_{x,\text{max}}$ increases with S .

Comparing with experiment, Fig. 8b, we see that the theoretically predicted cell length ($\Lambda = 2\pi/k_{x,\text{max}}$) consistently overestimates the experimentally observed cell lengths. Both show a linear dependence though, and for the experimental

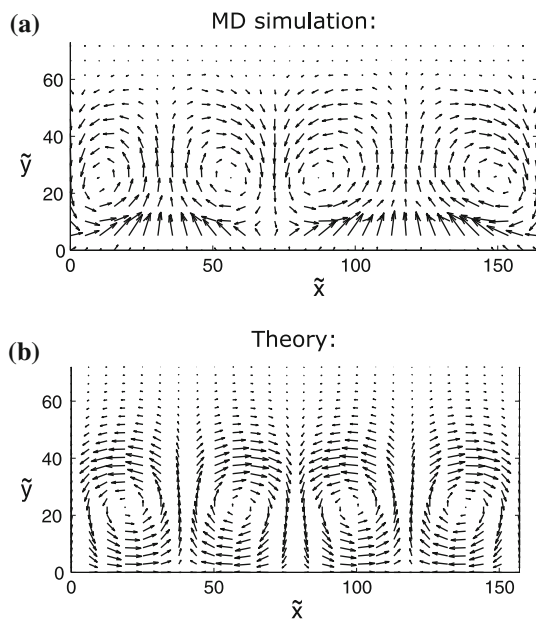


Fig. 11 MD simulation versus theory: **a** Velocity profile time averaged over 200 snapshots (i.e. 5 periods of the vibrating bottom) from a MD simulation with $F = 6.2$ layers in a container of length $L/d = 164$, shaken with an amplitude $a = 4.0$ mm and frequency $f = 52$ Hz ($S = 174$). **b** The theoretical velocity profile plotted for two cell lengths ($2\Lambda/d = 158$) for $F = 6$ layers and shaking strength $S = 170$

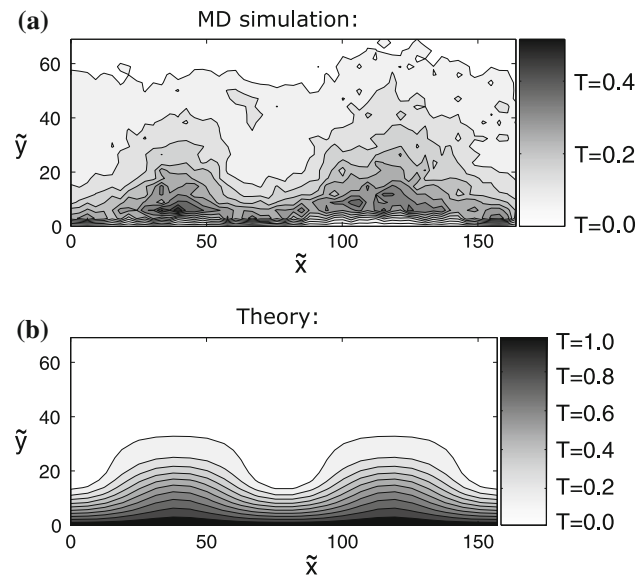


Fig. 12 MD simulation versus theory: **a** Time averaged temperature profile based on 200 snapshots from a MD simulation with $F = 6.2$ layers in a container of length $L/d = 164$, shaken at $a = 4.0$ mm and $f = 52$ Hz ($S = 174$). **b** Two cell lengths ($2\Lambda/d = 158$) of the theoretical temperature profile with $F = 6$ layers and shaking strength $S = 170$

data available the theoretical prediction becomes better for stronger fluidization.

The comparison of experiment, MD simulation and theory culminates in the (S, F) -phase diagram of Fig. 9 showing the

onset of convection for various numbers of layers⁴. Experiment, numerics and theory are seen to be in good agreement. The only fit parameter we have used is the Prandtl number of Eq. (12), the value of which we have fixed to $Pr = 1.7$ after fitting it to experimental data for $F = 8$.

5.2 Density profile

In Fig. 10 we compare the density profiles for experiment, MD simulation, and theory. The experimental density profile (Fig. 10a) is determined by averaging over 250 high-speed snapshots. The simulation profile (Fig. 10b) is time averaged over several snapshots, and averaged over the depth of the container. The density profiles of Fig. 10 are seen to reasonably agree.

In Fig. 7 we have shown how the experiments, simulations, and theory depend on the shaking strength S . The increasing cell length Λ for stronger fluidization has already been treated in the previous subsection. Besides, the cells also expand in height, which is an indication of the approaching transition from convection rolls to a granular gas.

In the theoretical density and velocity profiles, Fig. 7c, d, we have plotted two cell lengths Λ , determined by the value of $k_{x,max}$ of the dominant perturbation mode. If we translate these cell lengths to the experimental and numerical container length of $L/d = 101$, theory predicts that the container should contain $k = 2, 2,$ and 1 convective cells respectively. It exactly matches the results of the MD simulations and closely matches the experimental findings ($k = 3, 2$ and 1 respectively). So, the linear stability analysis of the hydrodynamic model is in reasonable quantitative agreement with the experiments and MD simulations.

5.3 Velocity profile

The velocity field cannot be extracted in a straightforward way from the experiment, because the particles overlap in the high-speed pictures of the quasi 2D setup. We therefore compare only the MD simulations with hydrodynamic theory, see Fig. 11. The velocity fields are very similar and display nearly the same cell length Λ .

5.4 Temperature profile

The granular temperature profile can be determined from the velocity field and because this data is only available for the MD simulations and hydrodynamic theory we compare these two in Fig. 12.

⁴ The results of Fig. 9 represent experiments with glass beads of $d = 1$ mm. Also for $F = 6.2$ layers of steel beads we found the onset of convection (at $S_{conv} = 62$) to match the theoretical prediction very well.

The theoretical temperature profile of Fig. 12b is determined in a similar manner as the theoretical density profile (Fig. 6): The perturbed temperature profile determined from the linear stability analysis is added to the temperature profile of the Leidenfrost state. Again, hydrodynamic theory and MD simulations match well.

6 Conclusion

We have studied buoyancy driven convection in vertically shaken granular matter, exploiting experiment, numerics, and hydrodynamic theory. At strong shaking strength counter-rotating convection rolls are formed, analogous to Rayleigh-Bénard convection for ordinary fluids with a free surface. Special features in our strongly shaken case are that the convection does not originate from a homogeneous fluid, but from the inhomogeneous Leidenfrost state (with a dense cluster floating on a gaseous region—but note again that granular convection roles can also arise without a prior density inversion as shown by Khain and Meerson [65]); neither does it originate from the interaction between the granulates and the walls, as in the case of weakly shaken granular matter, see e.g. [45]. Moreover, in our case the specific granular properties of the system can be expressed by constitutive relations.

In analogy with the theory of Rayleigh-Bénard convection in ordinary fluids [32] we have performed a linear stability analysis of the hydrodynamic model for this Leidenfrost state [28]. The results of this continuum description are found to be in good overall agreement with the experimental observations and simulations, and in particular the threshold in the (S, F) -phase diagram for the onset of convection (Fig. 9) shows a perfect match between experiment, simulation, and theory. This is a great success for granular hydrodynamics and stresses its applicability to collective phenomena in strongly shaken granular matter.

Future work will have to reveal the sensitivity of the results to the employed equation of state, constitutive relations, and transport coefficients in granular flow, which will allow to determine these relations and coefficients with considerably enhanced confidence. In parallel, some of these functions will be extracted from MD simulations directly. Moreover, in future work the approach of this present paper should be extended to higher dimensions, granular flow with smaller particles where the surrounding air becomes important, and particle mixtures of different sizes in which segregation starts to play a role.

Acknowledgments We would like to dedicate this paper to the memory of Professor Isaac Goldhirsch. We have discussed the issue of applicability of continuum equations to shaken granular matters many times with him, also in the context of this present work, and were always inspired by these discussions. His insight was deep and he was a real leader of the field. We would also like to thank Robert Bos for perform-

ing many of the experiments presented in this paper. This work is part of the research program of FOM, which is financially supported by NWO.

Appendix A: Alternative models for the shear viscosity μ

There is quite some discussion on the shear viscosity μ in granular systems and consequently various expressions have been proposed in the literature. Brey et al. [72] give the following relation for two dimensions and for a dilute granular gas:

$$\mu(T) = \frac{1}{2d} \sqrt{\frac{mT}{\pi}} \mu^*(e), \quad (61)$$

where $\mu^*(e)$ is a function of the restitution coefficient e .

Ohtsuki and Ohsawa [59] deduce an expression for μ including a dependence on the density n to account for excluded volume effects:

$$\mu(n, T) = \left\{ \frac{1}{4} n^2 d^3 + \frac{1}{2\pi d} \left(1 + \frac{\pi}{4} n d^2 \right)^2 \right\} \sqrt{\pi m T}. \quad (62)$$

He et al. [55] propose that the shear viscosity should be equal to the thermal conductivity κ :

$$\mu(n, T) = \kappa(n, T), \quad (63)$$

In the present paper we have found good correspondence between experiment and theory using a more general form based on dimension analysis:

$$\mu(n, T) = m \text{Pr} \kappa(n, T), \quad (64)$$

where Pr is the Prandtl number. We used it as a fit parameter for the phase diagram of Fig. 9 and found that Pr = 1.7 gave good agreement.

Figure 13 shows the influence of μ on the resulting growth rate $\gamma(k_x)$, comparing the results obtained if one uses the expression by Brey et al. (61) with those obtained for expression (64). It is seen that the viscosity definition of (64) has a stabilizing effect on the Leidenfrost state with increasing number of particle layers F , in agreement with the experimental observations, whereas (61) has a destabilizing effect. We show in the (S, F) -phase diagram of Fig. 9 that (64) yields qualitative and quantitative agreement with the experimental results.

Appendix B: Relations for the pressure, dissipation, and transport coefficients

For the matrix problem (51) we need to specify the elements of the matrices **A**, **B**, and **C** of (52)–(54), which contain p , I , and the transport coefficients and their derivatives. These are given below:

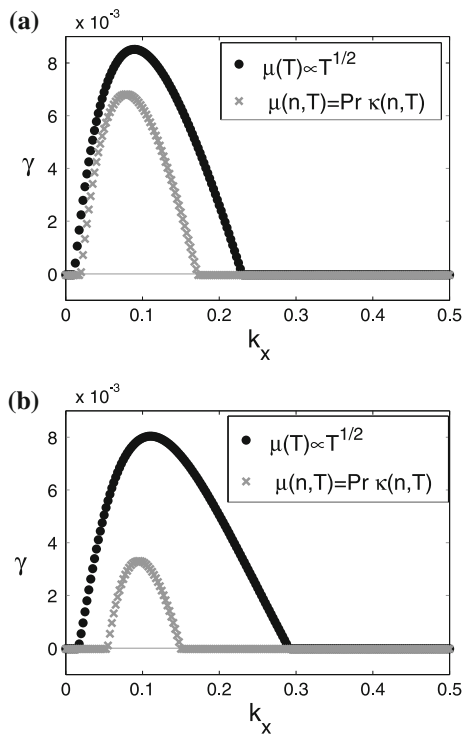


Fig. 13 *Theory*: Influence of the choice for the shear viscosity μ on the growth rate $\gamma(k_x)$ for two Leidenfrost states at the same shaking strength $S = 200$: **a** For $F = 6$ layers the region of instability of the Leidenfrost state is significantly reduced by going from the expression for $\mu(T)$ by Brey et al. [(61), black dots] to $\mu(n, T)$ as defined by (64) with $Pr = 1.7$ (grey crosses). **b** For $F = 11$ layers the stabilizing effect is even stronger. Note that the range of unstable k_x -values for the black dots has increased compared to the $F = 6$ Leidenfrost state, whereas the opposite is true for grey crosses

First of all, we have the equation of state for the pressure \tilde{p} and its derivatives:

$$\tilde{p}_L = \tilde{n}_L \tilde{T}_L \frac{1 + \tilde{n}_L}{1 - \tilde{n}_L}, \tag{65}$$

$$\frac{\partial \tilde{p}}{\partial \tilde{n}} \Big|_L = \tilde{T}_L \frac{1 + 2\tilde{n}_L - \tilde{n}_L^2}{(1 - \tilde{n}_L)^2}, \tag{66}$$

$$\frac{\partial}{\partial \tilde{y}} \left(\frac{\partial \tilde{p}}{\partial \tilde{n}} \Big|_L \right) = \frac{(1 - \tilde{n}_L)(1 + 2\tilde{n}_L - \tilde{n}_L^2) \frac{\partial \tilde{T}_L}{\partial \tilde{y}} + 4\tilde{T}_L \frac{\partial \tilde{n}_L}{\partial \tilde{y}}}{(1 - \tilde{n}_L)^3}, \tag{67}$$

$$\frac{\partial \tilde{p}}{\partial \tilde{T}} \Big|_L = \tilde{n}_L \frac{1 + \tilde{n}_L}{1 - \tilde{n}_L}, \tag{68}$$

$$\frac{\partial}{\partial \tilde{y}} \left(\frac{\partial \tilde{p}}{\partial \tilde{T}} \Big|_L \right) = \left[\frac{1 + 2\tilde{n}_L - \tilde{n}_L^2}{(1 - \tilde{n}_L)^2} \right] \frac{\partial \tilde{n}_L}{\partial \tilde{y}}. \tag{69}$$

The expressions for the energy dissipation rate \tilde{I} read as follows:

$$\tilde{I} = \frac{\varepsilon \tilde{n} \tilde{T}^{3/2}}{\gamma \tilde{\ell}}, \tag{70}$$

$$\frac{\partial \tilde{I}}{\partial \tilde{n}} \Big|_L = \frac{\varepsilon \tilde{T}^{3/2}}{\gamma} \left(\frac{\tilde{\ell} - \tilde{n} \frac{\partial \tilde{\ell}}{\partial \tilde{n}}}{\tilde{\ell}^2} \right), \tag{71}$$

$$\frac{\partial \tilde{I}}{\partial \tilde{T}} \Big|_L = \frac{3\varepsilon \tilde{n} \sqrt{\tilde{T}}}{2\gamma \tilde{\ell}}. \tag{72}$$

The mean free path $\tilde{\ell}$ and its derivatives are given by:

$$\tilde{\ell} = \sqrt{\frac{3}{32}} \left[\frac{1}{\tilde{n}} \left(\frac{1 - \tilde{n}}{1 - a\tilde{n}} \right) \right], \tag{73}$$

$$\frac{\partial \tilde{\ell}}{\partial \tilde{n}} = \sqrt{\frac{3}{32}} \left(\frac{-a\tilde{n}^2 + 2a\tilde{n} - 1}{\tilde{n}^2 (1 - a\tilde{n})^2} \right), \tag{74}$$

$$\frac{\partial^2 \tilde{\ell}}{\partial \tilde{n}^2} = 2\sqrt{\frac{3}{32}} \left(\frac{-a^2\tilde{n}^3 + 3a^2\tilde{n}^2 - 3a\tilde{n} + 1}{\tilde{n}^3 (1 - a\tilde{n})^3} \right). \tag{75}$$

We continue with the transport coefficient for the thermal conductivity $\tilde{\kappa}$ and its derivatives:

$$\tilde{\kappa}_L = \frac{(\alpha\tilde{\ell} + 1)^2}{\tilde{\ell}} \tilde{n} \sqrt{\tilde{T}}, \tag{76}$$

$$\frac{\partial \tilde{\kappa}_L}{\partial \tilde{y}} = \frac{\partial \tilde{\kappa}_L}{\partial \tilde{n}} \frac{\partial \tilde{n}}{\partial \tilde{y}} + \frac{\partial \tilde{\kappa}_L}{\partial \tilde{T}} \frac{\partial \tilde{T}}{\partial \tilde{y}}, \tag{77}$$

$$\frac{\partial \tilde{\kappa}}{\partial \tilde{n}} \Big|_L = \sqrt{\tilde{T}} \left[\frac{(\alpha\tilde{\ell} + 1)^2}{\tilde{\ell}} + \tilde{n} \frac{\alpha^2 \tilde{\ell}^2 - 1}{\tilde{\ell}^2} \frac{\partial \tilde{\ell}}{\partial \tilde{n}} \right], \tag{78}$$

$$\frac{\partial}{\partial \tilde{y}} \left(\frac{\partial \tilde{\kappa}}{\partial \tilde{n}} \Big|_L \right) = \frac{\partial}{\partial \tilde{n}} \left(\frac{\partial \tilde{\kappa}}{\partial \tilde{n}} \Big|_L \right) \frac{\partial \tilde{n}}{\partial \tilde{y}} + \frac{\partial}{\partial \tilde{T}} \left(\frac{\partial \tilde{\kappa}}{\partial \tilde{n}} \Big|_L \right) \frac{\partial \tilde{T}}{\partial \tilde{y}}, \tag{79}$$

$$\begin{aligned} & \frac{\partial}{\partial \tilde{n}} \left(\frac{\partial \tilde{\kappa}}{\partial \tilde{n}} \Big|_L \right) \\ &= \sqrt{\tilde{T}} \left[\frac{2(\alpha^2 \tilde{\ell}^2 - 1) \frac{\partial \tilde{\ell}}{\partial \tilde{n}} + \frac{2\tilde{n}}{\tilde{\ell}} \left(\frac{\partial \tilde{\ell}}{\partial \tilde{n}} \right)^2 + \tilde{n}(\alpha^2 \tilde{\ell}^2 - 1) \frac{\partial^2 \tilde{\ell}}{\partial \tilde{n}^2}}{\tilde{\ell}^2} \right]. \end{aligned} \tag{80}$$

$$\frac{\partial}{\partial \tilde{T}} \left(\frac{\partial \tilde{\kappa}}{\partial \tilde{n}} \Big|_L \right) = \frac{1}{2\sqrt{\tilde{T}}} \left[\frac{(\alpha\tilde{\ell} + 1)^2}{\tilde{\ell}} + \tilde{n} \frac{\alpha^2 \tilde{\ell}^2 - 1}{\tilde{\ell}^2} \frac{\partial \tilde{\ell}}{\partial \tilde{n}} \right], \tag{81}$$

$$\frac{\partial \tilde{\kappa}}{\partial \tilde{T}} \Big|_L = \frac{1}{2\sqrt{\tilde{T}_L}} \tilde{n} \frac{(\alpha\tilde{\ell} + 1)^2}{\tilde{\ell}}, \tag{82}$$

$$\frac{\partial}{\partial \tilde{y}} \left(\frac{\partial \tilde{\kappa}}{\partial \tilde{T}} \Big|_L \right) = \frac{\partial}{\partial \tilde{n}} \left(\frac{\partial \tilde{\kappa}}{\partial \tilde{T}} \Big|_L \right) \frac{\partial \tilde{n}}{\partial \tilde{y}} + \frac{\partial}{\partial \tilde{T}} \left(\frac{\partial \tilde{\kappa}}{\partial \tilde{T}} \Big|_L \right) \frac{\partial \tilde{T}}{\partial \tilde{y}}, \tag{83}$$

$$\frac{\partial}{\partial \tilde{n}} \left(\frac{\partial \tilde{\kappa}}{\partial \tilde{T}} \Big|_L \right) = \frac{1}{2\sqrt{\tilde{T}}} \left[\frac{(\alpha\tilde{\ell} + 1)^2}{\tilde{\ell}} + \tilde{n} \frac{\alpha^2 \tilde{\ell}^2 - 1}{\tilde{\ell}^2} \frac{\partial \tilde{\ell}}{\partial \tilde{n}} \right], \tag{84}$$

$$\frac{\partial}{\partial \tilde{T}} \left(\frac{\partial \tilde{\kappa}}{\partial \tilde{T}} \Big|_L \right) = -\frac{1}{4\tilde{T}\sqrt{\tilde{T}}} \tilde{n} \frac{(\alpha\tilde{\ell} + 1)^2}{\tilde{\ell}}. \tag{85}$$

References

1. Jenkins, J.T., Savage, S.B.: A theory for the rapid flow of identical, smooth, nearly elastic, spherical particles. *J. Fluid Mech.* **130**, 187 (1983)

2. Haff, P.K.: Grain flow as a fluid-mechanical phenomenon. *J. Fluid Mech.* **134**, 401 (1983)
3. Jenkins, J., Richman, M.: Boundary conditions for plane flows of smooth nearly elastic circular discs. *J. Fluid Mech.* **171**, 53 (1986)
4. Campbell, C.S.: Rapid granular flows. *Ann. Rev. Fluid Mech.* **22**, 57 (1990)
5. Jaeger, H.M., Nagel, S.R., Behringer, R.P.: Granular solids, liquids, and gases. *Rev. Mod. Phys.* **68**, 1259 (1996)
6. Behringer, R.P., Jaeger, H.M., Nagel, S.R.: The physics of granular materials. *Phys. Today* **49**, 32 (1996)
7. Sela, N., Goldhirsch, I.: Hydrodynamic equations for rapid flows of smooth inelastic spheres to Burnett order. *J. Fluid Mech.* **361**, 41 (1998)
8. Brey, J.J., Dufty, J.W., Kim, C.S., Santos, A.: Hydrodynamics for granular flow at low density. *Phys. Rev. E* **58**, 4638 (1998)
9. Kadanoff, L.P.: Built upon sand: theoretical ideas inspired by granular flows. *Rev. Mod. Phys.* **71**, 435 (1999)
10. Goldhirsch, I.: Rapid granular flows. *Annu. Rev. Fluid Mech.* **35**, 267 (2003)
11. Goldhirsch, I., Noskovicz, S., Bar-Lev, O.: Nearly smooth granular gases. *Phys. Rev. Lett.* **95**, 068002 (2005)
12. Du, Y., Li, H., Kadanoff, L.P.: Breakdown of hydrodynamics in a one-dimensional system of inelastic particles. *Phys. Rev. Lett.* **74**, 1268 (1995)
13. Sela, N., Goldhirsch, I.: Hydrodynamics of a one-dimensional granular medium. *Phys. Fluids* **7**, 507 (1995)
14. Duran, J.: *Sand, Powders and Grains: An Introduction to the Physics of Granular Materials*. Springer, New-York (1999)
15. Aranson, I.S., Tsimring, L.S.: Patterns and collective behavior in granular media: theoretical concepts. *Rev. Mod. Phys.* **78**, 641 (2006)
16. Goldhirsch, I., Zanetti, G.: Clustering instability in dissipative gases. *Phys. Rev. Lett.* **70**, 1619 (1993)
17. Kudrolli, A., Wolpert, M., Gollub, J.P.: Cluster formation due to collisions in granular material. *Phys. Rev. Lett.* **78**, 1383 (1997)
18. Eggers, J.: Sand as Maxwell's demon. *Phys. Rev. Lett.* **83**, 5322 (1999)
19. van der Weele, K., van der Meer, D., Versluis, M., Lohse, D.: Hysteretic custering in granular gas. *Europhys. Lett.* **53**, 328 (2001)
20. van der Meer, D., van der Weele, K., Lohse, D.: Sudden death of a granular cluster. *Phys. Rev. Lett.* **88**, 174302 (2002)
21. Alam, M., Nott, P.R.: Stability of plane couette flow of a granular material. *J. Fluid Mech.* **377**, 99 (1998)
22. Forterre, Y., Pouliquen, O.: Stability analysis of rapid granular chute flows: formation of longitudinal vortices. *J. Fluid Mech.* **467**, 361 (2002)
23. Alam, M.: Streamwise vortices and density patterns in rapid granular couette flow: a linear stability analysis. *J. Fluid Mech.* **553**, 1 (2006)
24. Lohse, D., Bergmann, R., Mikkelsen, R., Zeilstra, C., van der Meer, D., Versluis, M., van der Weele, K., van der Hoef, M., Kuipers, H.: Impact on soft sand: void collapse and jet formation. *Phys. Rev. Lett.* **93**, 198003 (2004)
25. Royer, J.R., Corwin, E.I., Flior, A., Cordero, M.L., Rivers, M.L., Eng, P.J., Jaeger, H.M.: Formation of granular jets observed by high-speed x-ray radiography. *Nat. Phys.* **1**, 164 (2005)
26. Kuipers, J.A.M.: Multilevel modelling of dispersed multiphase flows. *Oil Gas Sci. Technol. Rev. IFP* **55**, 427 (2000)
27. Eshuis, P., van der Meer, D., Alam, M., Gerner, H.J., van der Weele, K., Lohse, D.: Onset of convection in strongly shaken granular Matter. *Phys. Rev. Lett.* **104**, 038001 (2010)
28. Eshuis, P., van der Weele, K., van der Meer, D., Lohse, D.: Granular leidenfrost effect: experiment and theory of floating particle clusters. *Phys. Rev. Lett.* **95**, 258001 (2005)
29. Eshuis, P., van der Weele, K., van der Meer, D., Bos, R., Lohse, D.: Phase diagram of vertically shaken granular matter. *Phys. Fluids* **19**, 123301 (2007)
30. Normand, C., Porneau, Y., Velarde, M.G.: Convective instability: a physicist's approach. *Rev. Mod. Phys.* **49**, 581 (1977)
31. Swift, J., Hohenberg, P.C.: Hydrodynamic fluctuations at the convective instability. *Phys. Rev. E* **15**, 319 (1977)
32. Chandrasekhar, S.: *Hydrodynamic and Hydromagnetic Stability*. Dover, New-York (1981)
33. Bodenschatz, E., Pesch, W., Ahlers, G.: Recent developments in rayleigh-bénard convection. *Annu. Rev. Fluid Mech.* **32**, 709 (2000)
34. Rogers, J.L., Schatz, M.F., Bougie, J.L., Swift, J.B.: Rayleigh-bénard convection in a vertically oscillated fluid layer. *Phys. Rev. Lett.* **84**, 87 (2000)
35. Bormann, A.S.: The onset of convection in the rayleigh-bénard problem for compressible fluids. *Cont. Mech. Thermodyn.* **13**, 9 (2001)
36. Oh, J., Ahlers, G.: Thermal-noise effect on the transition to rayleigh-bénard convection. *Phys. Rev. Lett.* **91**, 094501 (2003)
37. Mutabazi, I., Guyon, E., Wesfreid, J.E.: *Dynamics of Spatio-Temporal Cellular Structures*, Henri Bénard Centenary Review, vol. 207. Springer, New York (2006)
38. Knight, J.B., Jaeger, H.M., Nagel, S.R.: Vibration-induced size separation in granular media: the convection connection. *Phys. Rev. Lett.* **70**, 3728 (1993)
39. Clément, E., Rajchenbach, J.: Fluidization of a bidimensional powder. *Europhys. Lett.* **16**, 133 (1991)
40. Gallas, J.A.C., Herrmann, H.J., Sokolowski, S.: Convection cells in vibrating granular media. *Phys. Rev. Lett.* **69**, 1371 (1992)
41. Taguchi, Y.-H.: Taguchi, New origin of a convective motion: Elastically induced convection in granular materials. *Phys. Rev. Lett.* **69**, 1367 (1992)
42. Luding, S., Clément, E., Blumen, A., Rajchenbach, J., Duran, J.: The onset of convection in molecular dynamics simulations of grains. *Phys. Rev. E* **50**, R1762 (1994)
43. Hayakawa, H., Yue, S., Hong, D.C.: Hydrodynamic description of granular convection. *Phys. Rev. Lett.* **75**, 2328 (1995)
44. Ehrichs, E.E., Jaeger, H.M., Karczmar, G.S., Knight, J.B., Kuperman, V.Y., Nagel, S.R.: Granular convection observed by magnetic resonance imaging. *Science* **267**, 1632 (1995)
45. Bourzutschky, M., Miller, J.: Granular convection in a vibrated fluid. *Phys. Rev. Lett.* **74**, 2216 (1995)
46. Aoki, K.M., Akiyama, T., Maki, Y., Watanabe, T.: Convective roll patterns in vertically vibrated beds of granules. *Phys. Rev. E* **54**, 874 (1996)
47. Knight, J.B., Ehrichs, E.E., Kuperman, V.Y., Flint, J.K., Jaeger, H.M., Nagel, S.R.: Experimental study of granular convection. *Phys. Rev. E* **54**, 5726 (1996)
48. Lan, Y., Rosato, A.D.: Convection related phenomena in granular dynamics simulations of vibrated beds. *Phys. Fluids* **9**, 3615 (1997)
49. Aoki, K.M., Akiyama, T.: Control parameter in granular convection. *Phys. Rev. E* **58**, 4629 (1998)
50. Bizon, C., Shattuck, M.D., Swift, J.B., McCormick, W.D., Swinney, H.L.: Patterns in 3d vertically oscillated granular layers: simulation and experiment. *Phys. Rev. Lett.* **80**, 57 (1998)
51. Ramírez, R., Risso, D., Cordero, P.: Thermal convection in fluidized granular systems. *Phys. Rev. Lett.* **85**, 1230 (2000)
52. Hsiao, S.S., Chen, C.H.: Granular convection cells in a vertical shaker. *Powder Technol.* **111**, 210 (2000)
53. Wildman, R.D., Huntley, J.M., Parker, D.J.: Convection in highly fluidized three-dimensional granular beds. *Phys. Rev. Lett.* **86**, 3304 (2001)
54. Sunthar, P., Kumaran, V.: Characterization of the stationary states of a dilute vibrofluidized granular bed. *Phys. Rev. E* **64**, 041303 (2001)

55. He, X., Meerson, B., Doolen, G.: Hydrodynamics of thermal granular convection. *Phys. Rev. E* **65**, 030301 (2002)
56. Garcimartin, A., Maza, D., Ilquimiche, J.L., Zuriguel, I.: Convective motion in a vibrated granular layer. *Phys. Rev. E* **65**, 031303 (2002)
57. Talbot, J., Viot, P.: Wall-enhanced convection in vibrofluidized granular systems. *Phys. Rev. Lett.* **89**, 064301 (2002)
58. Hsiau, S.S., Wang, P.C., Tai, C.H.: Convection cells and segregation in a vibrated granular bed. *AIChE J.* **48**, 1430 (2002)
59. Ohtsuki, T., Ohsawa, T.: Hydrodynamics for convection in vibrating beds of cohesionless granular materials. *J. Phys. Soc. Jpn.* **72**, 1963 (2003)
60. Cordero, P., Ramirez, R., Risso, D.: Buoyancy driven convection and hysteresis in granular gases: numerical solution. *Physica A* **327**, 82 (2003)
61. Miao, G., Huang, K., Yun, Y., Wei, R.: Active thermal convection in vibrofluidized granular systems. *Eur. Phys. J. B* **40**, 301 (2004)
62. Tai, C.H., Hsiau, S.S.: Dynamics behaviors of powders in a vibrating bed. *Powder Technol.* **139**, 221 (2004)
63. Risso, D., Soto, R., Godoy, S., Cordero, P.: Friction and convection in a vertically vibrated granular system. *Phys. Rev. E* **72**, 011305 (2005)
64. Isobe, M.: Bifurcations of a driven granular system under gravity. *Phys. Rev. E* **64**, 031304 (2001)
65. Khain, E., Meerson, B.: Onset of thermal convection in a horizontal layer of granular gas. *Phys. Rev. E* **67**, 021306 (2003)
66. Paolotti, D., Barrat, A., Marconi, U.M.B., Puglisi, A.: Thermal convection in monodisperse and bidisperse granular gases: a simulations study. *Phys. Rev. E* **69**, 061304 (2004)
67. Pak, H.K., Behringer, R.P.: Surface waves in vertically vibrated granular materials. *Phys. Rev. Lett.* **71**, 1832 (1993)
68. van der Hoef, M.A., Ye, M., van Sint Annaland, M., Andrews IV, A.T., Sundaresan, S., Kuipers, J.A.M.: Multi-scale modeling of gas-fluidized beds. *Adv. Chem. Eng.* **31**, 65 (2006)
69. Deen, N.G., van Sint Annaland, M., van der Hoef, M.A., Kuipers, J.A.M.: Review of discrete particle modeling of fluidized beds. *Chem. Eng. Sc.* **62**, 28 (2007)
70. Grossman, E.L., Zhou, T., Ben-Naim, E.: Towards granular hydrodynamics in two-dimensions. *Phys. Rev. E* **55**, 4200 (1997)
71. Meerson, B., Pöschel, T., Bromberg, Y.: Close-packed floating clusters: granular hydrodynamics beyond the freezing point? *Phys. Rev. Lett.* **91**, 024301 (2003)
72. Brey, J.J., Ruiz-Montero, M.J., Moreno, F.: Hydrodynamics of an open vibrated granular system. *Phys. Rev. E* **63**, 061305 (2001)
73. Garcia-Rojo, R., Luding, S., Brey, J.J.: Transport coefficients for dense hard-disk systems. *Phys. Rev. E* **74**, 061305 (2006)
74. Khain, E.: Hydrodynamics of fluid-solid coexistence in dense shear granular flow. *Phys. Rev. E* **75**, 051310 (2007)
75. Orszag, S.A.: Accurate solution of the orr-sommerfeld stability equation. *J. Fluid Mech.* **50**, 689 (1971)
76. Canuto, C., Hussaini, M.Y., Quarteroni, A., Zang, T.A.: *Spectral Methods: Fundamentals in Single Domains*. Springer, New York (2006)